3D Snake Robot Motion: Non-smooth Modeling, Simulations, and Experiments

Aksel A. Transeth, Remco I. Leine, Christoph Glocker, and Kristin Y. Pettersen

Abstract—A non-smooth (hybrid) 3D mathematical model of a snake robot (without wheels) is developed and experimentally validated in this paper. The model is based on the framework of non-smooth dynamics and convex analysis which allows us to easily and systematically incorporate unilateral contact forces (i.e. between the snake robot and the ground surface) and friction forces based on Coulomb's law of dry friction. Conventional numerical solvers can not be employed directly due to set-valued force laws and possible instantaneous velocity changes. Therefore, we show how to implement the model for numerical treatment with a numerical integrator called the time-stepping method. This method helps to avoid explicit changes between equations during simulation even though the system is hybrid. Simulation results for the serpentine motion pattern lateral undulation and sidewinding are presented. In addition, experiments are performed with the snake robot 'Aiko' for locomotion by lateral undulation and sidewinding, both with isotropic friction. For these cases, back-to-back comparisons between numerical results and experimental results are given.

Index Terms—Non-smooth dynamics, 3D snake robot, time-stepping method, kinematics.

I. INTRODUCTION

WHEELED mechanisms constitute the backbone of most ground-based means of transportation. Unfortunately, rough terrain makes it hard, if not impossible, for such mechanisms to move. To be able to move in various terrains, such as going through narrow passages and climb on rough ground, the high-mobility property of snakes is recreated in robots that look and move like snakes.

Snake robots most often have a high number of degrees of freedom (DOF) and they are able to move forward without using active wheels or legs. Due to the high number of DOF, it can be quite expensive and time-consuming to build and maintain a snake robot. This motivates the development of accurate mathematical models of snake robots. Such models can be used for synthesis and testing of various serpentine motion patterns intended for serpentine locomotion.

The first working snake robot was built in 1972 [1]. This robot was limited to planar motion, but snake robots capable of 3D motion have appeared more recently [2]–[6]. Together with the robots, mathematical models of both the kinematics

A. A. Transeth is with the Department of Applied Cybernetics at SINTEF ICT, NO-7465 Trondheim, Norway. Fax: +47 7359 4399 (e-mail: Aksel.Transeth@sintef.no).

R. I. Leine and Ch. Glocker are with the IMES-Centre of Mechanics, ETH Zürich, CH-8092 Zürich, Switzerland (e-mail:{Remco.Leine,Christoph.Glocker}@imes.mavt.ethz.ch).

K. Y. Pettersen is with the Department of Engineering Cybernetics at the Norwegian University of Science and Technology, NO-7491 Trondheim, Norway (e-mail: Kristin.Y.Pettersen@itk.ntnu.no).

Fig. 1. The NTNU/SINTEF snake robot 'Aiko'.

and the dynamics of snake robots have also been developed. Purely kinematic 3D models have been presented in [6]–[8], where frictional contact between the snake robot and the ground is not included in the model. Hence, contact between the snake robot and the ground surface is either modeled with frictionless passive wheels, or the parts of the snake robot that touches the ground are defined as anchored to the ground [9]. A model of the dynamics of motion is needed to describe the friction forces a snake robot without wheels is subjected to when moving over a surface. Most mathematical models that describe the dynamics of snake robot motion have been limited to planar (2D) motion [10]– [13], and 3D mathematical models of snake robots have only recently been developed [3], [7]. 3D models facilitate testing and development of 3D serpentine motion patterns such as sinus-lifting and sidewinding. A description of these motion patterns is found in e.g. [4]. A physics engine called the Open Dynamics Engine (ODE) has been employed to simulate a 15-link snake robot instead of deriving explicit expressions for its dynamics in [14]. Such software makes it easy to change the geometry of a snake robot if needed and the time needed to prepare a working model is relatively short [15].

On a flat surface, the ability of a snake robot to move forward is dependent on the friction between the ground surface and the body of the snake robot. Hence, unilateral contact forces and friction forces are important parts of the mathematical model of a snake robot. The friction forces have usually been based on a Coulomb or viscous-like friction model [11], [12], and Coulomb friction has most often been modeled using a sign-function [12], [16]. Contact between a snake robot and the ground surface can sometimes be approximated by a no-sideways-slip constraint for snake robot with wheels [17], [18]. However, such an approximation is not valid for wheel-less snake robots. The unilateral contact forces have been modeled as a mass-spring-damper system in [3] (i.e. compliant contact) and each link has only a single and fixed contact point with the ground surface. When running simulations, direct implementations or approximations

of the sign-function can lead to an erroneous description of sticking contacts or very stiff differential equations. Also, a mass-spring-damper model introduces a very stiff spring that leads to stiff differential equations. In addition, it is not clear how to determine the dissipation parameters of the contact unambiguously when using a compliant model [19]. The Open Dynamics Engine implements a form of rigid body contact (i.e. not compliant contact). However, the implementation of this engine trades off simulation accuracy in order to increase simulation speed and stability [15], [20].

In this paper, we develop a non-smooth (hybrid) 3D mathematical model of a snake robot with cylindrical links without wheels. *Set-valued* force laws for the constitutive description of unilateral contact forces and friction forces in a three-dimensional setting are described in the framework of non-smooth dynamics and convex analysis [19], [21], [22]. Moreover, the model has a moving contact point on the *surface* of each link for contact with the ground surface instead of just a fixed point for each link. The latter is an approach employed in prior publications on mathematical models of 3D snake robot motion. Stick-slip transitions (based on a set-valued Coulomb friction law) and impacts with the ground are modeled as instantaneous transitions. This results in an accurate model of *spatial* Coulomb friction where both the direction of the friction force and a true stick-phase are taken properly into account. For wheel-less snake robots it is important to describe the frictional contact between the wheel-less snake robot and the ground in an accurate manner, both with respect to stick-slip transitions and the direction of the friction force while sliding along the ground surface. This latter property also distinguishes wheel-less snake robots from e.g. legged mechanisms which most often try to 'stick' to the ground rather than sliding along it. The dynamics of the snake robot is described by an equality of measures, which includes the Newton-Euler equations for the non-impulsive part of the motion as well as impact equations. A particular choice of coordinates results in an effective way of writing the system equations. The set-valuedness of the force laws allows us to write each constitutive law with a single equation and avoids explicit switching between equations (for example when a collision between the snake robot and the ground surface occurs) even though this is a hybrid system. This is advantageous since the snake robot links repeatedly collides with the ground surface during e.g. locomotion by sidewinding. A discretization of the equality of measures gives the so-called time-stepping method (see [22] and references therein) which we use for numerical simulation. The description of the model and the method for numerical integration are presented in this paper in such a way that people who are new to the field of non-smooth dynamics can use this paper as an introduction to non-smooth modeling of robot manipulators with impacts and friction. In addition, we present experimental results that validate the mathematical model. To the best of our knowledge, this is the first time such a back-to-back comparison between simulation and experimental results is presented for 3D snake robot motion. The experiments are performed with the snake robot 'Aiko' in Fig. 1 built at the NTNU/SINTEF Advanced Robotics Laboratory.

The paper is organised as follows. A short introduction to the modeling procedure is given in Section II. The kinematics of the snake robot with the ground surface as a unilateral constraint is described in Section III. Then, the groundwork for finding the friction and ground contact forces is laid in Section IV. The non-smooth dynamics is presented in Section V, while the serpentine motion patterns employed in this paper are described in Section VI. The numerical treatment of the mathematical model is given in Section VII. Simulations and experimental validations are given in Section VIII. Conclusions and suggestions for further research are presented in Section IX.

II. SUMMARY OF THE MATHEMATICAL MODEL

This section contains a brief outline of how to derive the non-smooth mathematical model of the snake robot. This preliminary section is meant to motivate and ease the understanding of the forthcoming deduction of the system equations.

The snake robot model consists of n links connected by $n-1$ two-degrees-of-freedom (DOF) cardan joints (i.e. rotational joints). Let $u \in \mathbb{R}^{6n}$ be a vector containing the translational and rotational velocities of all the links of the snake robot (the structure of the snake robot together with the coordinates and reference frames are described further in Section III). Let the differential measures $\mathrm{d}u$ and $\mathrm{d}t$ be loosely described for now as a 'possible differential change' in u and time t, respectively, while a more precise definition is given in Section V. The use of differential measures allows for instantaneous changes in velocities which occurs for impacts between the snake robot and the ground surface. The system equations for the snake robot can now be written as

$$\mathbf{M}\mathrm{d}u - h\mathrm{d}t - \mathrm{d}\boldsymbol{R} = \boldsymbol{\tau}_C\mathrm{d}t, \qquad (1)$$

which is called the *equality of measures* [23], where $\mathbf{M} \in \mathbb{R}^{6n \times 6n}$ is the mass matrix, $h \in \mathbb{R}^{6n}$ consists of the smooth forces, $\boldsymbol{\tau}_C \in \mathbb{R}^{6n}$ contains all the joint actuator torques, and $\mathrm{d}\boldsymbol{R} \in \mathbb{R}^{6n}$ accounts for the normal contact forces/impulses from the ground, the Coulomb friction forces/impulses, and the bilateral constraint forces/impulses in the joints. Note: We allow in this paper for *instantaneous* changes in velocities usually associated with collisions. Hence, the (normal contact/friction/constraint) *forces* are not always defined due to the infinite accelerations. In these cases we have *impulses* instead of forces. The non-smooth equality of measures (1) allows us to formulate in a uniform manner both the smooth and non-smooth phases of motion. This is achieved partly by representing the contact forces/impulses as *contact impulse measures*.

A substantial part of the beginning of this paper is devoted to deducting the force measure $\mathrm{d}\boldsymbol{R}$. Hence, let us briefly look at how to derive the contribution of the normal contact impulse measure between the ground and the first link, in $\mathrm{d}\boldsymbol{R}$. Let $\mathrm{d}\boldsymbol{R}_1 \in \mathbb{R}^6$ be the sum of contact impulse measures that directly affects link 1 (i.e the six top elements of $\mathrm{d}\boldsymbol{R}$), then

$$\mathrm{d}\boldsymbol{R}_1 = \boldsymbol{w}_N \, \mathrm{d}P_N + \left\{ \begin{array}{l} \text{friction and joint constraint} \\ \text{impulse measures} \end{array} \right\}, \quad (2)$$

where $dP_N \in \mathbb{R}$ is the normal contact impulse measure from the ground on link 1, and $\boldsymbol{w}_N \in \mathbb{R}^6$ is the corresponding generalised force direction, i.e. a Jacobian (subscripts 'j' and '1' are omitted for brevity).

Let $g_N \in \mathbb{R}$ be a function giving the shortest distance between the rear part of link 1 and the ground. Such a function is called a *gap function* [24]. The gap function is the starting point for the systematic approach of finding the impulse measures. The ground and the rear part of the link are separated if $g_N > 0$, are in contact if $g_N = 0$, and are penetrating each other if $g_N < 0$. Now, the relative velocity between link 1 and the ground along the shortest line between the two objects can be defined as

$$\gamma_N := \boldsymbol{w}_N^{\mathrm{T}} \boldsymbol{u}_1, \tag{3}$$

where $\boldsymbol{u}_1$ is the velocity of link 1, and $\boldsymbol{w}_N = \partial g_N / \partial \boldsymbol{q}$ is the generalised force direction used in (2). It holds that $\gamma_N = \dot{g}_N$ for almost all t. The normal contact impulse measure dP_N is related to the relative velocity γ_N through a *set-valued force law* (see Section V-B1). The set-valuedness of the force laws allows us to write each constitutive law (force law) with a single equation and avoids explicit switching between equations (for example when a collision occurs). In addition, this formulation provides an accurate description of the planar Coulomb friction (see Section V-B2). In the following three sections, we will elaborate on how to derive the elements that constitute (1), that is the various gap functions, relative velocities, and finally the forces/impulses which appear in the equality of measures.

III. KINEMATICS

The kinematics describes the geometrical aspect of motion. From the geometry of the snake robot, we develop *gap functions* for ground contact detection. These functions are also needed for calculating the directions of the contact forces.

This section will first give an overview of the coordinates used to describe the position and orientation of the snake robot. Subsequently, the gap functions will be presented.

A. Coordinates and Reference Frames

The snake robot model consists of n cylindrical links that are connected by $n-1$ cardan joints, each having two degrees of freedom (DOF). The distance L_i between two adjacent cardan joints equals the length of link i, and the radius of each link is L_{SC_i}. Each link is modelled as a cylinder of length $2L_{GS_i}$ with two spheres of radius L_{SC_i} attached to the ends the link. Link i with parts of its two adjacent links are illustrated in Fig. 2.

We denote an earth-fixed coordinate frame $I = (O, \boldsymbol{e}_x^I, \boldsymbol{e}_y^I, \boldsymbol{e}_z^I)$, see Fig. 2, as an approximation to an inertial frame where its centre O is fixed to the ground surface and the $\boldsymbol{e}_z^I$-axis is pointing in the opposite direction of the acceleration of gravity vector $\boldsymbol{g} = \begin{bmatrix} 0 & 0 & -g \end{bmatrix}^{\mathrm{T}}$. We denote a body-fixed frame $B_i = (G_i, \boldsymbol{e}_x^I, \boldsymbol{e}_y^I, \boldsymbol{e}_z^I)$, where G_i is the centre of gravity of link i (which coincides with the geometric centre of the link-cylinder) and $\boldsymbol{e}_z^I$ points along the centre line of link i toward link $i+1$.
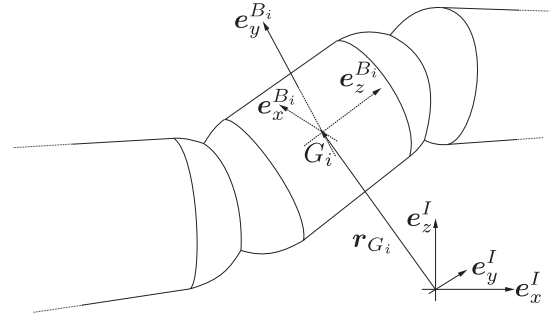

Fig. 2. Reference frames.

The position and orientation of link i are described by the *non-minimal absolute* coordinates [25]

$$\boldsymbol{q}_i = \begin{bmatrix} {}_I \boldsymbol{r}_{G_i} \\ \boldsymbol{p}_i \end{bmatrix} \in \mathbb{R}^7, \tag{4}$$

where ${}_I \boldsymbol{r}_{G_i} = \begin{bmatrix} x_i & y_i & z_i \end{bmatrix}^{\mathrm{T}} \in \mathbb{R}^3$ is the position of the centre of gravity of link i and the vector $\boldsymbol{p}_i = \begin{bmatrix} e_{i_0} & \boldsymbol{e}_i^{\mathrm{T}} \end{bmatrix}^{\mathrm{T}}$, where $\boldsymbol{e}_i^{\mathrm{T}} = \begin{bmatrix} e_{i_1} & e_{i_2} & e_{i_3} \end{bmatrix}$, contains the four Euler parameters used to describe the rotation. The Euler parameters form a unit quaternion vector with the constraint $\boldsymbol{p}_i^{\mathrm{T}} \boldsymbol{p}_i = 1$. The coordinates are *non-minimal* because each link is described with 6 coordinates, and *absolute* because the position and orientation of link i is given directly relative to frame I. The velocity of link i is given by

$$\boldsymbol{u}_i = \begin{bmatrix} {}_I \boldsymbol{v}_{G_i} \\ {}_{B_i} \boldsymbol{\omega}_{IB_i} \end{bmatrix} \in \mathbb{R}^6, \tag{5}$$

where ${}_I \boldsymbol{v}_{G_i}$ is the translational velocity of the CG of link i which is ${}_I \boldsymbol{v}_{G_i} = {}_I \dot{\boldsymbol{r}}_{G_i}$ when it exists (i.e. for impact free motion). Moreover, ${}_{B_i} \boldsymbol{\omega}_{IB_i}$ is the angular velocity of frame B_i relative to frame I, given in frame B_i. The transformation ${}_I \boldsymbol{r} = \mathbf{R}_{B_i}^I {}_{B_i} \boldsymbol{r}$ can be performed with the rotation matrix $\mathbf{R}_{B_i}^I = \mathbf{H}_i \bar{\mathbf{H}}_i^{\mathrm{T}}$ where

$$\mathbf{H}_i = \begin{bmatrix} -\boldsymbol{e}_i & \tilde{\boldsymbol{e}}_i + e_{i_0} \mathbf{I} \end{bmatrix}, \ \bar{\mathbf{H}}_i = \begin{bmatrix} -\boldsymbol{e}_i & -\tilde{\boldsymbol{e}}_i + e_{i_0} \mathbf{I} \end{bmatrix}, \tag{6}$$

and the superscript $\tilde{}$ denotes the skew-symmetric form of a vector throughout this paper, i.e.

$$\tilde{\boldsymbol{e}} = \begin{bmatrix} 0 & -e_{i_3} & e_{i_2} \\ e_{i_3} & 0 & -e_{i_1} \\ -e_{i_2} & e_{i_1} & 0 \end{bmatrix}. \tag{7}$$

The time-derivative of the rotation matrix is found from [26] as

$$\dot{\mathbf{R}}_{B_i}^I = \mathbf{R}_{B_i}^I {}_{B_i} \tilde{\boldsymbol{\omega}}_{IB_i} = {}_I \tilde{\boldsymbol{\omega}}_{IB_i} \mathbf{R}_{B_i}^I. \tag{8}$$

The coordinates (positions and orientation) and velocities of all links are gathered in the vectors $\boldsymbol{q} = \begin{bmatrix} \boldsymbol{q}_1^{\mathrm{T}} & \cdots & \boldsymbol{q}_n^{\mathrm{T}} \end{bmatrix}^{\mathrm{T}}$ and $\boldsymbol{u} = \begin{bmatrix} \boldsymbol{u}_1^{\mathrm{T}} & \cdots & \boldsymbol{u}_n^{\mathrm{T}} \end{bmatrix}^{\mathrm{T}}$.

B. Gap Functions for Unilateral Constraints

Gap functions for the unilateral constraints (i.e. the ground surface) give the minimal distance between the floor and the front and rear part of each link. The contact surfaces between
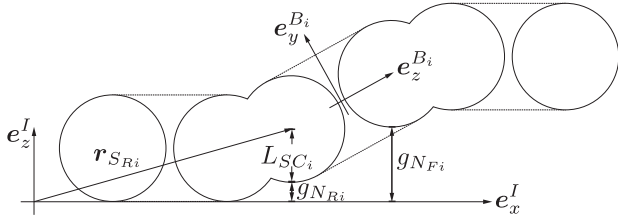
Fig. 3. Surfaces (solid-drawn circles) on snake robot that constitute the contact between the robot and the ground.

a link and the ground are modeled as two spheres at the ends of the link as illustrated for a three-link robot in Fig. 3.

We denote the distance between the centre of the two spheres that belong to link i by $2L_{GS_i}$ and the radius of the spheres by L_{SC_i}. The position of the centre of the front and rear spheres are denoted by $\boldsymbol{r}_{S_{Fi}}$ and $\boldsymbol{r}_{S_{Ri}}$, respectively. The shortest distance between the ground and the points on the front and rear spheres closest to the ground are denoted by $g_{N_{Fi}}$ and $g_{N_{Ri}}$, respectively. The distances are found from

$$g_{N_{Fi}} = (\boldsymbol{r}_{S_{Fi}})^{\mathrm{T}} \boldsymbol{e}_z^I - L_{SC_i}, \ g_{N_{Ri}} = (\boldsymbol{r}_{S_{Ri}})^{\mathrm{T}} \boldsymbol{e}_z^I - L_{SC_i}, \quad (9)$$

where $\boldsymbol{r}_{S_{Fi}} = \boldsymbol{r}_{G_i} + L_{GS_i} \boldsymbol{e}_z^{B_i}$, $\boldsymbol{r}_{S_{Ri}} = \boldsymbol{r}_{G_i} - L_{GS_i} \boldsymbol{e}_z^{B_i}$.

The gap functions are gathered in the vector

$$\boldsymbol{g}_N = \begin{bmatrix} g_{N_{F1}} & \cdots & g_{N_{Fn}} & g_{N_{R1}} & \cdots & g_{N_{Rn}} \end{bmatrix}^{\mathrm{T}}. \quad (10)$$

C. Gap Functions for Bilateral Constraints

Each 2 DOF cardan joint introduces four bilateral constraints, which will be described by gap functions.

To find the translational 'gap' in the joints, we need to relate the position of the joint between link i and $i+1$ to both links. Let the position of the joint between link i and $i+1$ be written as $_I\boldsymbol{r}_{J_{Fi}} = {_I\boldsymbol{r}_{G_i}} + \frac{1}{2}L_i {_I\boldsymbol{e}_z^{B_i}}$, $_I\boldsymbol{r}_{J_{Ri+1}} = {_I\boldsymbol{r}_{G_{i+1}}} - \frac{1}{2}L_i {_I\boldsymbol{e}_z^{B_{i+1}}}$. The gap functions can now be found from

$$g_{J_{i\chi}} = \left({_I\boldsymbol{r}_{J_{Fi}}} - {_I\boldsymbol{r}_{J_{Ri+1}}} \right)^{\mathrm{T}} {_I\boldsymbol{e}_\chi^I}, \quad (11)$$

for $i = 1, \ldots, n-1$, and $\chi = x, y, z$. Hence,

$$g_{J_{i\chi}} = \left({_I\boldsymbol{r}_{G_i}} - {_I\boldsymbol{r}_{G_{i+1}}} \right)^{\mathrm{T}} {_I\boldsymbol{e}_\chi^I} \quad (12)$$
$$+ \frac{1}{2} \left(L_i \mathbf{R}_{B_i}^I {_{B_i}\boldsymbol{e}_z^{B_i}} + L_{i+1} \mathbf{R}_{B_{i+1}}^I {_{B_{i+1}}\boldsymbol{e}_z^{B_{i+1}}} \right)^{\mathrm{T}} {_I\boldsymbol{e}_\chi^I}$$

for $i = 1, \ldots, n-1$.

The next gap function provides a 'gap' in rotation around the axis that a cardan joint is not able to rotate around. Let $\boldsymbol{e}_y^{B_i}$ and $\boldsymbol{e}_x^{B_{i+1}}$ be the axes of rotation for the cardan joint between link i and link $i+1$, then $\left(\boldsymbol{e}_y^{B_i} \right)^{\mathrm{T}} \boldsymbol{e}_x^{B_{i+1}} = 0$. Hence, a measure for the rotational 'gap' can be defined from the equality above as the gap function

$$g_{J_{i\phi}} = \left(\mathbf{R}_{B_i}^I {_{B_i}\boldsymbol{e}_y^{B_i}} \right)^{\mathrm{T}} \left(\mathbf{R}_{B_{i+1}}^I {_{B_{i+1}}\boldsymbol{e}_x^{B_{i+1}}} \right). \quad (13)$$

IV. CONTACT CONSTRAINTS ON VELOCITY LEVEL

In this section we calculate relative velocities between the snake robot and the ground from the gap functions. The relative velocities are needed to set up the set-valued contact forces for the closed contacts [27].

A. Unilateral Contact: Ground Contact

Contact between the snake robot and the ground involves (vertical) normal forces, which guarantee the unilaterality of the contact, and (horizontal) tangential contact forces, which are due to friction and are dependent on the normal contact forces and the relative sliding velocities.

1) Relative Velocities Along $\boldsymbol{e}_z^I$: The relative velocities between the front and rear part of link i and the ground along the $\boldsymbol{e}_z^I$-axis are defined as $\gamma_{N_{Fi}} := \dot{g}_{N_{Fi}}$ and $\gamma_{N_{Ri}} := \dot{g}_{N_{Ri}}$ (when they exist), respectively, and they are used later to find the normal contact forces. Before we proceed, note that $\gamma_{N_{Fi}}$ (or $\gamma_{N_{Ri}}$) should not be found directly by taking the time-derivative of the expression for $g_{N_{Fi}}$ (or $g_{N_{Fi}}$) in (9). This is the case since the expressions (9) have already been simplified due to the fact that expressions have been inserted for the various body-fixed vectors which constitute the gap functions. Instead, for the relative velocities, we must consider the velocity of a *body-fixed* point P_{Fi} which at time-instant t coincides with a point C_{Fi} on the front sphere closest to the ground (the same principle applies for the rear part of the link). Note that the position vectors for P_{F_i} and C_{F_i} will be the same instantaneously. However, the *differentials* will be different. This is shown in the following. Let C_{Fi} be a point on the front sphere that moves on the sphere such that the point is always closest to the ground surface. Then the position of this point is

$$\boldsymbol{r}_{C_{Fi}} = \boldsymbol{r}_{G_i} + \boldsymbol{r}_{G_i S_{Fi}} + \boldsymbol{r}_{S_{Fi} C_{Fi}}. \quad (14)$$

Define the skew-symmetric matrix $_I\tilde{\boldsymbol{r}}_{G_i C_{Fi}} = {_I\tilde{\boldsymbol{r}}_{G_i S_{Fi}}} + {_I\tilde{\boldsymbol{r}}_{S_{Fi} C_{Fi}}}$. The velocity of the point C_{Fi} is obtained by differentiation of (14):

$$_I\boldsymbol{v}_{C_{Fi}} = \underbrace{{_I\boldsymbol{v}_{G_i}} - {_I\tilde{\boldsymbol{r}}_{G_i C_{Fi}}} \mathbf{R}_{B_i}^I {_{B_i}\boldsymbol{\omega}_{IB_i}}}_{_I\boldsymbol{v}_{P_{Fi}}} + \mathbf{R}_{B_i}^I {_{B_i}\dot{\boldsymbol{r}}_{S_{Fi} C_{Fi}}}, \quad (15)$$

where we now can use that

$$\boldsymbol{r}_{S_{Fi} C_{Fi}} = -L_{SC_i} \boldsymbol{e}_z^I, \quad (16)$$

and we have employed (8) and $_{B_i}\dot{\boldsymbol{r}}_{G_i S_{Fi}} = 0$, together with the identities $_I\tilde{\boldsymbol{\omega}}_{IB_i} {_I\boldsymbol{r}_{G_i S_{Fi}}} = -{_I\boldsymbol{\omega}_{IB_i}} {_I\tilde{\boldsymbol{r}}_{G_i S_{Fi}}}$ and $_I\tilde{\boldsymbol{\omega}}_{IB_i} {_I\boldsymbol{r}_{S_{Fi} C_{Fi}}} = -{_I\boldsymbol{\omega}_{IB_i}} {_I\tilde{\boldsymbol{r}}_{S_{Fi} C_{Fi}}}$. We see from (15) an expression for the velocity $_I\boldsymbol{v}_{P_{Fi}}$ of the body-fixed point P_{Fi} which at time-instance t coincides with the point C_{Fi}. This velocity will be employed to find both the relative velocities along $\boldsymbol{e}_z^I$ and the tangential relative velocities. The equivalent velocity $_I\boldsymbol{v}_{P_{Ri}}$ on the rear part of the sphere is found similarly to $_I\boldsymbol{v}_{P_{Fi}}$ in (15) by replacing Fi by Ri in (15)-(16).

Now, the relative velocities along $\boldsymbol{e}_z^I$ for the front and rear part of link i can be found as

$$\gamma_{N_{Qi}} = \left({_I\boldsymbol{e}_z^I} \right)^{\mathrm{T}} {_I\boldsymbol{v}_{P_{Qi}}} \implies \gamma_{N_{Qi}} = (\boldsymbol{w}_{N_{Qi}})^{\mathrm{T}} \boldsymbol{u}_i, \quad (17)$$

where

$$\boldsymbol{w}_{N_{Qi}} = \left[({_I\boldsymbol{e}_z^I})^{\mathrm{T}} \quad -({_I\boldsymbol{e}_z^I})^{\mathrm{T}} {_I\tilde{\boldsymbol{r}}_{G_i C_{Qi}}} \mathbf{R}_{B_i}^I \right]^{\mathrm{T}}, \quad (18)$$

for $Q = F, R$ with $\boldsymbol{r}_{G_i S_{Fi}} = L_{GS_i} \boldsymbol{e}_z^{B_i}$ and $\boldsymbol{r}_{G_i S_{Ri}} = -L_{GS_i} \boldsymbol{e}_z^{B_i}$. The motivation to use the form (17) is that $\boldsymbol{w}_{N_{Qi}}$ gives the generalised direction of the contact force between the ground and the front and rear part of link i.

A vector gathering all $\gamma_{N_{Fi}}$ and $\gamma_{N_{Ri}}$ is

$$\boldsymbol{\gamma}_N = \mathbf{W}_N^{\mathrm{T}} \boldsymbol{u}, \tag{19}$$

where $\boldsymbol{\gamma}_N = \begin{bmatrix} \gamma_{N_{F1}} & \cdots & \gamma_{N_{Fn}} & \gamma_{N_{R1}} & \cdots & \gamma_{N_{Rn}} \end{bmatrix}^{\mathrm{T}}$, $\mathbf{W}_N = \begin{bmatrix} \mathbf{W}_{N_F} & \mathbf{W}_{N_R} \end{bmatrix} \in \mathbb{R}^{6n \times 2n}$, and

$$\mathbf{W}_{N_Q} = \begin{bmatrix} \boldsymbol{w}_{N_{Q1}} & \mathbf{0}_{6\times 1} & \cdots & \mathbf{0}_{6\times 1} \\ \mathbf{0}_{6\times 1} & \ddots & & \vdots \\ \vdots & & \ddots & \mathbf{0}_{6\times 1} \\ \mathbf{0}_{6\times 1} & \cdots & \mathbf{0}_{6\times 1} & \boldsymbol{w}_{N_{Qn}} \end{bmatrix}, \tag{20}$$

for $Q = F, R$.

2) Tangential Relative Velocities: Friction forces between a link and the ground depend on the relative velocities in the $(\boldsymbol{e}_x^I, \boldsymbol{e}_y^I)$-plane between the snake robot links and the ground. These velocities are termed tangential relative velocities. First, the relative velocities between the front part of link i and the ground along the $\boldsymbol{e}_x^I$- and $\boldsymbol{e}_y^I$-axis, $\gamma'_{T_{Fix}}$ and $\gamma'_{T_{Fiy}}$, will be deducted. Subsequently, the relative velocities for the front part of link i along the projection of the longitudinal axis of the link onto the $(\boldsymbol{e}_x^I, \boldsymbol{e}_y^I)$-plane $\gamma_{T_{Fix}}$ and transversal to the link $\gamma_{T_{Fiy}}$, will be deducted from $\gamma'_{T_{Fix}}$ and $\gamma'_{T_{Fiy}}$ respectively. The same type of notation applies for the rear part of link i: $\gamma'_{T_{Rix}}$, $\gamma'_{T_{Riy}}$, $\gamma_{T_{Rix}}$ and $\gamma_{T_{Riy}}$. The tangential relative velocities are found much in the same way as for $\gamma_{N_{Fi}}$ and $\gamma_{N_{Ri}}$. Consequently, we find the velocities of the points P_{Fi} and P_{Ri} along the $\boldsymbol{e}_x^I$- and $\boldsymbol{e}_y^I$-axis. Hence, by looking at (17), we see that the tangential relative velocities of the contact points on the front part of the link can be found as

$$\gamma'_{T_{Fi\zeta}} = ({}_I\boldsymbol{e}_\zeta^I)^{\mathrm{T}} {}_I\boldsymbol{v}_{P_{Fi}} \Longrightarrow \gamma'_{T_{Fi\zeta}} = (\boldsymbol{w}'_{T_{Fi\zeta}})^{\mathrm{T}} \boldsymbol{u}_i, \tag{21}$$

for $\zeta = x, y$, where

$$\boldsymbol{w}'_{T_{Fi\zeta}} = \begin{bmatrix} ({}_I\boldsymbol{e}_\zeta^I)^{\mathrm{T}} & -({}_I\boldsymbol{e}_\zeta^I)^{\mathrm{T}} {}_I\tilde{\boldsymbol{r}}_{G_iC_{Fi}} \mathbf{R}_{B_i}^I \end{bmatrix}^{\mathrm{T}}. \tag{22}$$

The relative velocities between the rear part of the link and the ground are found by exchanging ${}_I\boldsymbol{v}_{P_{Fi}}$ with ${}_I\boldsymbol{v}_{P_{Ri}}$ in (21):

$$\gamma'_{T_{Ri\zeta}} = ({}_I\boldsymbol{e}_\zeta^I)^{\mathrm{T}} {}_I\boldsymbol{v}_{P_{Ri}} \Longrightarrow \gamma'_{T_{Ri\zeta}} = (\boldsymbol{w}'_{T_{Ri\zeta}})^{\mathrm{T}} \boldsymbol{u}_i, \tag{23}$$

for $\zeta = x, y$, where

$$\boldsymbol{w}'_{T_{Ri\zeta}} = \begin{bmatrix} ({}_I\boldsymbol{e}_\zeta^I)^{\mathrm{T}} & -({}_I\boldsymbol{e}_\zeta^I)^{\mathrm{T}} {}_I\tilde{\boldsymbol{r}}_{G_iC_{Fi}} \mathbf{R}_{B_i}^I \end{bmatrix}^{\mathrm{T}}. \tag{24}$$

The tangential relative velocities for the front and rear part of the link i are combined in vectors:

$$\boldsymbol{\gamma}'_{T_{Qi}} = \mathbf{W}'^{\mathrm{T}}_{T_{Qi}} \boldsymbol{u}_i, \tag{25}$$

for $Q = F, R$, where $\boldsymbol{\gamma}'_{T_{Qi}} = \begin{bmatrix} \gamma'_{T_{Qix}} & \gamma'_{T_{Qiy}} \end{bmatrix}^{\mathrm{T}}$ and

$$\mathbf{W}'_{T_{Qi}} = \begin{bmatrix} \boldsymbol{w}'_{T_{Qix}} & \boldsymbol{w}'_{T_{Qiy}} \end{bmatrix} \in \mathbb{R}^{6\times 2}. \tag{26}$$

Until now the relative velocities have been given in the directions along the $\boldsymbol{e}_x^I$ and $\boldsymbol{e}_y^I$ axes. In order to calculate the friction forces longitudinal and transversal to a link, we need to know the corresponding relative velocities in these directions in the $(\boldsymbol{e}_x^I, \boldsymbol{e}_y^I)$-plane. To calculate these velocities we introduce for each link a frame Π_i with axes $(\boldsymbol{e}_x^{\Pi_i}, \boldsymbol{e}_y^{\Pi_i}, \boldsymbol{e}_z^{\Pi_i})$, where ${}_I\boldsymbol{e}_z^{\Pi_i} = {}_I\boldsymbol{e}_z^I$, and

$${}_I\boldsymbol{e}_x^{\Pi_i} = \frac{\mathbf{A}_{xy} {}_I\boldsymbol{e}_z^{B_i}}{\|\mathbf{A}_{xy} {}_I\boldsymbol{e}_z^{B_i}\|}, \quad {}_I\boldsymbol{e}_y^{\Pi_i} = \frac{{}_I\boldsymbol{e}_z^I \times {}_I\boldsymbol{e}_x^{\Pi_i}}{\|{}_I\boldsymbol{e}_z^I \times {}_I\boldsymbol{e}_x^{\Pi_i}\|}, \tag{27}$$

where $\mathbf{A}_{xy} = \mathrm{diag}([1, 1, 0])$. Hence, it holds that

$$\mathbf{R}_{\Pi_i}^I = \begin{bmatrix} {}_I\boldsymbol{e}_x^{\Pi_i} & {}_I\boldsymbol{e}_y^{\Pi_i} & {}_I\boldsymbol{e}_z^{\Pi_i} \end{bmatrix}. \tag{28}$$

Notice that ${}_I\boldsymbol{e}_x^{\Pi_i} = {}_I\boldsymbol{e}_z^{B_i}$ and ${}_I\boldsymbol{e}_y^{\Pi_i} = {}_I\boldsymbol{e}_x^{B_i}$ when link i is lying flat on the ground with ${}_I\boldsymbol{e}_y^{B_i} = {}_I\boldsymbol{e}_z^I$. Since only the motion in the $(\boldsymbol{e}_x^I, \boldsymbol{e}_y^I)$-plane is of interest, we define

$$\bar{\mathbf{R}}_{\Pi_i}^I = \mathbf{D}^{\mathrm{T}} \mathbf{R}_{\Pi_i}^I \mathbf{D}, \quad \mathbf{D} = \begin{bmatrix} 1 & 0 & 0 \\ 0 & 1 & 0 \end{bmatrix}^{\mathrm{T}}. \tag{29}$$

Since we now have that $\boldsymbol{\gamma}'_{T_{Qi}} = \bar{\mathbf{R}}_{\Pi_i}^I \boldsymbol{\gamma}_{T_{Qi}}$, $Q = F, R$, the relative velocity between the floor and the front part of link i, with respect to frame Π_i, can be found from (25) as

$$\boldsymbol{\gamma}_{T_{Qi}} = \mathbf{W}_{T_{Qi}}^{\mathrm{T}} \boldsymbol{u}_i, \tag{30}$$

where $\boldsymbol{\gamma}_{T_{Qi}} = \begin{bmatrix} \gamma_{T_{Qix}} & \gamma_{T_{Qiy}} \end{bmatrix}^{\mathrm{T}}$, $\mathbf{W}_{T_{Qi}} = \mathbf{W}'_{T_{Qi}} \bar{\mathbf{R}}_{\Pi_i}^I$, for $Q = F, R$.

A vector that gathers all $\boldsymbol{\gamma}_{T_{Fi}}$ and $\boldsymbol{\gamma}_{T_{Ri}}$ is found from

$$\boldsymbol{\gamma}_T = \mathbf{W}_T^{\mathrm{T}} \boldsymbol{u}, \tag{31}$$

where

$$\boldsymbol{\gamma}_T = \begin{bmatrix} \boldsymbol{\gamma}_{T_{F1}}^{\mathrm{T}} & \cdots & \boldsymbol{\gamma}_{T_{Fn}}^{\mathrm{T}} & \boldsymbol{\gamma}_{T_{R1}}^{\mathrm{T}} & \cdots & \boldsymbol{\gamma}_{T_{Rn}}^{\mathrm{T}} \end{bmatrix}^{\mathrm{T}}, \tag{32}$$

$\mathbf{W}_T = \begin{bmatrix} \mathbf{W}_{T_F} & \mathbf{W}_{T_R} \end{bmatrix} \in \mathbb{R}^{6n \times 4n}$, and $\mathbf{W}_{T_F}, \mathbf{W}_{T_R}$ are found similarly to (20) by replacing the zero-vectors with $\mathbf{0}_{6\times 2}$ and replacing the vectors $\boldsymbol{w}_{N_{Fi}}, \boldsymbol{w}_{N_{Ri}}$ with the matrices $\mathbf{W}_{T_{Fi}}, \mathbf{W}_{T_{Ri}}$, respectively.

3) Relative Rolling Velocities: Up until now, we have only considered translational relative motion of the snake robot links. However, we also need to consider rotational relative motion to add a damping effect on the rotational motion in the form of rotational friction. In order to do this, we introduce a relative rolling velocity as

$$\boldsymbol{\gamma}_{V_{Qi}} = \mathbf{D}^{\mathrm{T}} \left({}_I\boldsymbol{r}_{C_{Qi}S_{Qi}} \times {}_I\boldsymbol{\omega}_{IB_i} \right), \tag{33}$$

for $Q = F, R$, where $\boldsymbol{\gamma}_{V_{Qi}} = \begin{bmatrix} \gamma_{V_{Qix}} & \gamma_{V_{Qiy}} \end{bmatrix}^{\mathrm{T}}$ and ${}_I\boldsymbol{r}_{C_{Qi}S_{Qi}} = L_{SC_i} {}_I\boldsymbol{e}_z^I$ is the vector pointing (upwards) from the body-fixed point C_{Q_i} on the link end-sphere momentarily closest to the ground, towards the centre S_{Q_i} of the end-sphere. By employing the identity

$${}_I\boldsymbol{r}_{C_{Qi}S_{Qi}} \times {}_I\boldsymbol{\omega}_{IB_i} = {}_I\tilde{\boldsymbol{r}}_{C_{Qi}S_{Qi}} \mathbf{R}_{B_i}^I {}_{B_i}\boldsymbol{\omega}_{IB_i}, \tag{34}$$

we find that the relative rolling velocity can be written

$$\boldsymbol{\gamma}_{V_{Qi}} = \mathbf{W}_{V_{Qi}}^{\mathrm{T}} \boldsymbol{u}_i, \tag{35}$$

where

$$\mathbf{W}_{V_{Qi}}^{\mathrm{T}} = \begin{bmatrix} \mathbf{O}_{2\times 3} & \mathbf{D}^{\mathrm{T}} {}_I\tilde{\boldsymbol{r}}_{C_{Qi}S_{Qi}} \mathbf{R}_{B_i}^I \end{bmatrix}, \tag{36}$$

for $Q = F, R$.

We gather all the relative rolling velocities as

$$\boldsymbol{\gamma}_V = \mathbf{W}_V \boldsymbol{u}, \tag{37}$$

where $\boldsymbol{\gamma}_V = \begin{bmatrix} \boldsymbol{\gamma}_{V_{F1}}^{\mathrm{T}} & \cdots & \boldsymbol{\gamma}_{V_{Fn}}^{\mathrm{T}} & \boldsymbol{\gamma}_{V_{R1}}^{\mathrm{T}} & \cdots & \boldsymbol{\gamma}_{V_{Rn}}^{\mathrm{T}} \end{bmatrix}^{\mathrm{T}}$, $\mathbf{W}_V = \begin{bmatrix} \mathbf{W}_{V_F} & \mathbf{W}_{V_R} \end{bmatrix} \in \mathbb{R}^{6n \times 4n}$, and $\mathbf{W}_{V_F}, \mathbf{W}_{V_R}$ are found similarly to (20) by replacing the zero-vectors with $\mathbf{0}_{6\times 2}$ and replacing the vectors $\boldsymbol{w}_{N_{Fi}}, \boldsymbol{w}_{N_{Ri}}$ with the matrices $\mathbf{W}_{V_{Fi}}, \mathbf{W}_{V_{Ri}}$, respectively.

B. Bilateral Constraints: Joints

Bilateral constraints introduced by the cardan joint between two adjacent links prohibit relative motion between the links in four DOF. The relative velocities between the links along these DOF need to be found in order to calculate the bilateral constraint forces in the joints. These relative velocities are found from the gap functions (12) and (13).

Relative velocities for the translational gap between link i and link $i+1$ are defined as $\gamma_{J_{i_\chi}} := \dot{g}_{J_{i_\chi}}$ for $i = 1, \ldots, n-1$ where $\chi = x, y, z$. By employing (12), we find that

$$\gamma_{J_{i_\chi}} = \boldsymbol{w}_{J_{i_\chi}}^{\mathrm{T}} \begin{bmatrix} \boldsymbol{u}_i \\ \boldsymbol{u}_{i+1} \end{bmatrix}, \tag{38}$$

where

$$\boldsymbol{w}_{J_{i_\chi}} = \begin{bmatrix} ({}_I\boldsymbol{e}_\chi^I) \\ -\left(({}_I\boldsymbol{e}_\chi^I)^{\mathrm{T}} \frac{L_i}{2} \mathbf{R}_{B_i}^I \, {}_{B_i}\tilde{\boldsymbol{e}}_z^{B_i}\right)^{\mathrm{T}} \\ -({}_I\boldsymbol{e}_\chi^I) \\ -\left(({}_I\boldsymbol{e}_\chi^I)^{\mathrm{T}} \frac{L_{i+1}}{2} \mathbf{R}_{B_{i+1}}^I \, {}_{B_{i+1}}\tilde{\boldsymbol{e}}_z^{B_{i+1}}\right)^{\mathrm{T}} \end{bmatrix}. \tag{39}$$

A relative velocity for the rotational gap is defined as $\gamma_{J_{i\phi}} := \dot{g}_{J_{i\phi}}$ for $i = 1, \ldots, n-1$. Hence,

$$\gamma_{J_{i\phi}} = \boldsymbol{w}_{J_{i\phi}}^{\mathrm{T}} \begin{bmatrix} \boldsymbol{u}_i \\ \boldsymbol{u}_{i+1} \end{bmatrix}, \tag{40}$$

where

$$\boldsymbol{w}_{J_{i\phi}} = \begin{bmatrix} \mathbf{0}_{3\times 1} \\ -\left(\mathbf{R}_{B_i}^I \, {}_{B_i}\tilde{\boldsymbol{e}}_y^{B_i}\right)^{\mathrm{T}} \left(\mathbf{R}_{B_{i+1}}^I \, {}_{B_{i+1}}\boldsymbol{e}_x^{B_{i+1}}\right) \\ \mathbf{0}_{3\times 1} \\ -\left(\mathbf{R}_{B_{i+1}}^I \, {}_{B_{i+1}}\tilde{\boldsymbol{e}}_x^{B_{i+1}}\right)^{\mathrm{T}} \left(\mathbf{R}_{B_i}^I \, {}_{B_i}\boldsymbol{e}_y^{B_i}\right) \end{bmatrix}. \tag{41}$$

Let $\boldsymbol{\gamma}_{J_i} = \begin{bmatrix} \gamma_{J_{ix}} & \gamma_{J_{iy}} & \gamma_{J_{iz}} & \gamma_{J_{i\phi}} \end{bmatrix}^{\mathrm{T}}$, then we can gather all the relative velocities concerned with the bilateral constraints in one vector

$$\boldsymbol{\gamma}_J = \mathbf{W}_J^{\mathrm{T}} \boldsymbol{u}, \tag{42}$$

where $\boldsymbol{\gamma}_J = \begin{bmatrix} \boldsymbol{\gamma}_{J_1}^{\mathrm{T}} & \cdots & \boldsymbol{\gamma}_{J_{n-1}}^{\mathrm{T}} \end{bmatrix}^{\mathrm{T}}$,

$$\mathbf{W}_J = \begin{bmatrix} \mathbf{W}_{J1}^{\mathrm{T}} & \mathbf{0}_{4\times 6} & \cdots & \mathbf{0}_{4\times 6} \\ \mathbf{0}_{4\times 6} & \mathbf{W}_{J2}^{\mathrm{T}} & & \vdots \\ \vdots & & \ddots & \mathbf{0}_{4\times 6} \\ \mathbf{0}_{4\times 6} & \cdots & \mathbf{0}_{4\times 6} & \mathbf{W}_{Jn-1}^{\mathrm{T}} \end{bmatrix}^{\mathrm{T}} \in \mathbb{R}^{6n\times 4(n-1)}, \tag{43}$$

and $\mathbf{W}_{Ji} = \begin{bmatrix} \boldsymbol{w}_{J_{ix}} & \boldsymbol{w}_{J_{iy}} & \boldsymbol{w}_{J_{iz}} & \boldsymbol{w}_{J_{i\phi}} \end{bmatrix} \in \mathbb{R}^{12\times 4}$ for $i = 1, \ldots, n-1$.

V. NON-SMOOTH DYNAMICS

The starting point for describing the dynamics of the snake robot is the *equality of measures* as introduced in [23]. The equality of measures includes equations of motion for impact free motion as well as impact equations. The impact equations give rise to impulsive behaviour [24]. In this section, we employ the results from Section III and IV in order to find the equality of measures for the snake robot.

A. The Equality of Measures

An equality of measures describes the dynamics of the snake robot within the context of non-smooth dynamics. Velocity jumps, usually associated with impacts, are modeled to occur instantaneously. Hence, the time-derivative of a velocity does not always exist. By considering the generalised velocity to be a function $t \mapsto \boldsymbol{u}(t)$ of locally bounded variation on a time-interval $I = [t_A, t_E]$ [23], the function $\boldsymbol{u}(t)$ admits a right $\boldsymbol{u}^+$ and left $\boldsymbol{u}^-$ limit for all $t \in I$, and its time-derivative $\dot{\boldsymbol{u}}$ exists for almost all $t \in I$. To be able to obtain $\boldsymbol{u}$ from integration we need to use the differential measure $\mathrm{d}\boldsymbol{u}$ where it is assumed that the measure can be decomposed into

$$\mathrm{d}\boldsymbol{u} = \dot{\boldsymbol{u}}\mathrm{d}t + \left(\boldsymbol{u}^+ - \boldsymbol{u}^-\right)\mathrm{d}\eta, \tag{44}$$

where $\mathrm{d}t$ denotes the Lebesgue measure and $\mathrm{d}\eta$ denotes the atomic measure where $\int_{\{t_1\}} \mathrm{d}\eta = 1$. The total increment of $\boldsymbol{u}$ over a compact subinterval $[t_1, t_2]$ of I, is found as

$$\int_{[t_1,t_2]} \mathrm{d}\boldsymbol{u} = \boldsymbol{u}^+(t_2) - \boldsymbol{u}^-(t_1), \tag{45}$$

and is due to a continuous change (i.e. impact free motion) stemming from $\dot{\boldsymbol{u}}$ as well as possible discontinuities in $\boldsymbol{u}$ due to impacts within the time-interval $[t_1, t_2]$. Equation (45) is also valid when the time-interval reduces to a singleton $\{t_1\}$, and if a velocity jump occurs for $t = t_1$ then (45) gives a nonzero result.

From the notation above, the Newton-Euler equations as an equality of measures can be written in a general form as

$$\mathbf{M}(\boldsymbol{q},t)\,\mathrm{d}\boldsymbol{u} - \boldsymbol{h}(\boldsymbol{q},\boldsymbol{u},t)\,\mathrm{d}t - \mathrm{d}\boldsymbol{R} = \boldsymbol{\tau}_C\mathrm{d}t, \tag{46}$$

where the mass matrix $\mathbf{M}(\boldsymbol{q},t)$, the vector of smooth forces $\boldsymbol{h}(\boldsymbol{q},\boldsymbol{u},t)$, the force measure of possibly atomic impact impulsions $\mathrm{d}\boldsymbol{R}$, and the vector of applied torques $\boldsymbol{\tau}_C$ will be described in the following.

For our choice of coordinates, the mass matrix is *diagonal* and constant

$$\mathbf{M}(\boldsymbol{q},t) = \mathbf{M} = \begin{bmatrix} \mathbf{M}_1 & & \mathbf{0} \\ & \ddots & \\ \mathbf{0} & & \mathbf{M}_n \end{bmatrix} \in \mathbb{R}^{6n\times 6n}, \tag{47}$$

where

$$\mathbf{M}_i = \begin{bmatrix} m_i\mathbf{I}_{3\times 3} & \mathbf{0}_{3\times 3} \\ \mathbf{0}_{3\times 3} & {}_{B_i}\boldsymbol{\Theta}_{G_i} \end{bmatrix}, \tag{48}$$

with ${}_{B_i}\boldsymbol{\Theta}_{G_i} = \mathrm{diag}\left(\begin{bmatrix} \Theta_{1i} & \Theta_{1i} & \Theta_{3i} \end{bmatrix}\right)$, m_i is the mass of link i, and Θ_{1i} and Θ_{3i} are its moments of inertia. The smooth forces, here consisting of gravity and gyroscopic accelerations, are described by $\boldsymbol{h}(\boldsymbol{q},\boldsymbol{u},t) = \boldsymbol{h}(\boldsymbol{u}) = \begin{bmatrix} \boldsymbol{h}_1^{\mathrm{T}}(\boldsymbol{u}_1) & \cdots & \boldsymbol{h}_n^{\mathrm{T}}(\boldsymbol{u}_n) \end{bmatrix}^{\mathrm{T}} \in \mathbb{R}^{6n}$, where $\boldsymbol{h}_i(\boldsymbol{u}_i) = \begin{bmatrix} 0 & 0 & -m_ig & -\left({}_{B_i}\tilde{\boldsymbol{\omega}}_{IB_i}\,{}_{B_i}\boldsymbol{\Theta}_{G_i}\,{}_{B_i}\boldsymbol{\omega}_{IB_i}\right)^{\mathrm{T}} \end{bmatrix}^{\mathrm{T}}$.

The force measure $\mathrm{d}\boldsymbol{R}$ accounts for all the contact forces and impulses. The contact efforts that constitute $\mathrm{d}\boldsymbol{R}$ are found from the force-laws given in Section V-B. Let $\mathcal{I}$ be the set of all active contacts with the ground

$$\mathcal{I}(t) = \{a \mid g_{N_a}(\boldsymbol{q}(t)) = 0\} \subseteq \{1, 2, \ldots, 2n\}, \tag{49}$$

where g_{N_a} is the a-th element of the vector $\boldsymbol{g}_N$ in (10). Now, the force measure is written as

$$
\begin{aligned}
\mathrm{d}\boldsymbol{R} =& \mathbf{W}_J\,\mathrm{d}\boldsymbol{P}_J + \sum_{a\in\mathcal{I}}(\mathbf{W}_N)_a\,\mathrm{d}P_{N_a} \\
&+ \sum_{a\in\mathcal{I}}\big((\mathbf{W}_T)_{2a-1}\,\mathrm{d}P_{T_{ax}} + (\mathbf{W}_T)_{2a}\,\mathrm{d}P_{T_{ay}}\big) \\
&+ \sum_{a\in\mathcal{I}}\big((\mathbf{W}_V)_{2a-1}\,\mathrm{d}P_{V_{ax}} + (\mathbf{W}_V)_{2a}\,\mathrm{d}P_{V_{ay}}\big),
\end{aligned}
\tag{50}
$$

where $\mathrm{d}P_{N_a}$ is the normal contact impulse measure between the ground and a link, $\mathrm{d}P_{T_{ax}}$ and $\mathrm{d}P_{T_{ay}}$ are the tangential contact impulse measures (friction) between the floor and a link, longitudinal and transversal to the link (i.e. along the $\boldsymbol{e}_x^{\Pi_i}$- and $\boldsymbol{e}_y^{\Pi_i}$-axis), respectively, $\mathrm{d}P_{V_{ax}}$ and $\mathrm{d}P_{V_{ay}}$ are the rotational contact impulse measures (friction) between the floor and a link, along the $\boldsymbol{e}_x^{I}$-axis and $\boldsymbol{e}_y^{I}$-axis, respectively, $\mathrm{d}\boldsymbol{P}_J$ is the contact impulse measure due to the bilateral constraints in the joints (these constraints are always active), and the lower-case subscripts on the $\mathbf{W}$-matrices indicate which column of the matrix is used. The position of the elements of the vectors $\mathrm{d}\boldsymbol{P}_N$, $\mathrm{d}\boldsymbol{P}_J$, $\mathrm{d}\boldsymbol{P}_T$, and $\mathrm{d}\boldsymbol{P}_V$ corresponds to the position of the elements in their respective vector of relative velocity $\boldsymbol{\gamma}_N$, $\boldsymbol{\gamma}_J$, $\boldsymbol{\gamma}_T$, and $\boldsymbol{\gamma}_V$. Hence, looking at for example the expression (32) for $\boldsymbol{\gamma}_T$, we see that e.g. $\mathrm{d}\boldsymbol{P}_{T_{n+1}} = \big[\mathrm{d}P_{T_{(n+1)x}}\ \mathrm{d}P_{T_{(n+1)y}}\big]^{\mathrm{T}}$ corresponds to $\boldsymbol{\gamma}_{T_{R1}}$, and we know from this that $\mathrm{d}\boldsymbol{P}_{T_{n+1}}$ is the tangential contact impulse measure between the ground and the rear part of link 1.

The contact impulse measures can be decomposed in the same way as for $\mathrm{d}\boldsymbol{u}$. Let us take the normal contact impulse measure as an example. The measure can be written as

$$
\mathrm{d}P_{N_a} = \lambda_{N_a}\mathrm{d}t + \Lambda_{N_a}\mathrm{d}\eta, \tag{51}
$$

where λ_{N_a} is the Lebesgue-measurable force and Λ_{N_a} is the purely atomic impact impulse. The same decomposition can also be performed for the three other impulse measures.

The control torques $\boldsymbol{\tau}_C$ are described in Section V-C below.

B. Constitutive Laws for the Contact Forces

In this section, we will introduce set-valued force laws for normal contact and Coulomb friction. These laws will all be formulated on velocity level using the relative contact velocities $\boldsymbol{\gamma}$ given by (19) and (31). Subsequently, the set-valued force laws are formulated as equalities in Section V-B4 using the so-called 'proximal point function' in order to include the force laws in the numerical simulation [22].

1) Normal Contact Force: The normal contact between a link and the floor is described by the unilateral constraint

$$
g_N \geq 0,\ \lambda_N \geq 0,\quad g_N\lambda_N = 0, \tag{52}
$$

which is known as Signorini's law [22]. Here, λ_N is the normal contact force and g_N is the gap function. Subscripts Ri and Fi are temporarily removed for simplicity. This set-valued force law states that the contact is impenetrable, $g_N \geq 0$, the contact can only transmit pressure forces $\lambda_N \geq 0$ and the contact force λ_N does not produce work $g_N\lambda_N = 0$. The force law can be expressed on different kinematic levels: displacement level (52), velocity level, and acceleration level.

In the following we express all force laws for closed contact on velocity level, while all forces vanish for open contacts. Then, by employing concepts of convex analysis, the relationship between the relative velocity and the Lebesgue measurable normal contact force (not an impulse) may be written for a closed contact $g_N = 0$ as an inclusion on velocity level

$$
-\gamma_N \in N_{C_N}(\lambda_N), \tag{53}
$$

where the convex set $C_N = \{\lambda_N \mid \lambda_N \geq 0\} = \mathbb{R}^+$ is the set of admissible contact forces, and N_{C_N} is the normal cone to C_N [22]. The inclusion (53) is equivalent to the condition

$$
\gamma_N \geq 0,\ \lambda_N \geq 0,\quad \gamma_N\lambda_N = 0, \tag{54}
$$

for a closed contact $g_N = 0$. Before explaining the above force law (53), let us first mention that this force law describes impenetrability of sustained contact, i.e. $g_N = 0$ and $\gamma_N = 0$, as well as detachment: $\gamma_N > 0 \Rightarrow \lambda_N = 0$. However, (53) does not cover impacts (where we have impulses instead of forces). For impacts we need a similar *impact law* described at the end of this subsection.

From the definition [22], [28] of a normal cone $N_C(\boldsymbol{x})$ to a convex set C at the point $\boldsymbol{x} \in \mathbb{R}^n$, we have that $N_C(\boldsymbol{x}) = \{0\}$ for $\boldsymbol{x} \in \mathrm{int}\,C$, and $N_C(\boldsymbol{x}) = \{\emptyset\}$ for $\boldsymbol{x} \notin C$. If $\boldsymbol{x}$ is on the *boundary* of C, then $N_C(\boldsymbol{x})$ is the set of all vectors $\boldsymbol{y} \in \mathbb{R}^n$ that are normal to $\boldsymbol{x}$. For example, for $C_N = \mathbb{R}^+$ we have $N_{C_N}(0) = \mathbb{R}^-$ and $N_{C_N}(2) = 0$.

The force law (53) only covers finite-valued contact efforts during impulse free motion, i.e. all velocities are absolutely continuous in time. When a collision occurs in a rigid-body setting, then the velocities will be locally discontinuous in order to prevent penetration. The velocity jump is accompanied by an impact impulse Λ_N, for which we will set up an impact law. The relative velocity admits, similarly to the velocities $\boldsymbol{u}$, a right γ_N^+ and a left γ_N^- limit. The impact law for a completely inelastic impact at a closed contact can now be written as

$$
-\gamma_N^+ \in N_{C_N}(\Lambda_N),\qquad C_N = \{\Lambda_N \mid \Lambda_N \geq 0\} = \mathbb{R}^+, \tag{55}
$$

which is equivalent to the condition

$$
\gamma_N^+ \geq 0,\ \Lambda_N \geq 0,\quad \gamma_N^+\Lambda_N = 0. \tag{56}
$$

Notice that the force law (53) and impact law (55) is on the same form. We have earlier stated that there is no need for an explicit switch between equations when e.g. and impact occurs. This becomes evident in Section VII with the introduction of the contact impulse (that includes both forces and possible impulses) for the discretization of the system dynamics.

The force law for normal contact given in this section can also be employed to describe normal contact with obstacles. This is described in [29].

2) Coulomb Friction Force: In this section, we describe the friction force between the snake robot and the ground when the snake robot slides along the ground surface as set-valued Coulomb friction. Similarly to the force law (53) for normal contact, we describe the constitutive description for friction using an inclusion on a normal cone. The friction force $\boldsymbol{\lambda}_T$,
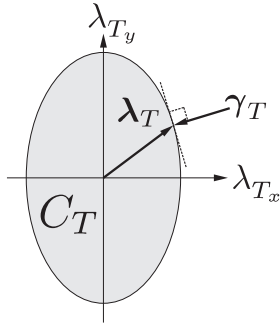
Fig. 4. Relationship between tangential relative velocity and friction force. The set C_T is in grey.

in the two-dimensional tangent plane to the contact point, is modeled with an anisotropic Coulomb friction law

$$-\boldsymbol{\gamma}_T \in N_{C_T}(\boldsymbol{\lambda}_T), \qquad (57)$$

where $\boldsymbol{\gamma}_T$ is a relative sliding velocity, N_{C_T} is the normal cone to the set C_T, and the ellipse

$$C_T = \left\{ \boldsymbol{\lambda}_T \mid \frac{\lambda_{T_x}^2}{(\mu_{T_x}\lambda_N)^2} + \frac{\lambda_{T_y}^2}{(\mu_{T_y}\lambda_N)^2} \leq 1 \right\}, \qquad (58)$$

is the set of admissible friction forces, where $\boldsymbol{\lambda}_T = \begin{bmatrix} \lambda_{T_x} & \lambda_{T_y} \end{bmatrix}^T$, and μ_{T_x}, $\mu_{T_y} > 0$ are directional friction coefficients along the $\boldsymbol{e}_x^\Pi$- and $\boldsymbol{e}_y^\Pi$-axis from (27), respectively. Fig. 4 depicts the set C_T (in grey), together with the relationship between the tangential relative velocities and the friction force when it is on the boundary of C_T.

The force law (57) distinguishes between two cases: if the friction force is in the interior of C_T or on its boundary. If $\boldsymbol{\lambda}_T \in \text{int}\, C_T$, then it holds that $N_{C_T}(\boldsymbol{\lambda}_T) = \boldsymbol{0}$ from which we conclude that $\boldsymbol{\gamma}_T = \boldsymbol{0}$. Obviously, this corresponds to the stick phase of the friction law. If the friction force is on the boundary of C_T, then the normal cone $N_{C_T}(\boldsymbol{\lambda}_T)$ consists of the outward normal ray on the ellipse C_T at the point $\boldsymbol{\lambda}_T$.

The advantage to formulate the friction law as the inclusion (57) now becomes apparent. First of all, note that (57), is a *spatial* friction law. Such a spatial friction law can not properly be described by a set-valued sign-function. Some authors [10], [12] model the spatial contact with two sign-functions for the two components of the relative sliding velocity using two friction coefficients μ_{T_x} and μ_{T_y}. Others smoothen the (set-valued) sign function with a smoothening function, e.g. some arctangent function. This results in a very steep slope of the friction curve near zero relative velocity. Such an approach is very cumbersome for two reasons. First of all, stiction can not properly be described: an object on a slope will with a smoothened friction law always slide. Secondly, the very steep slope of the friction curve causes the differential equations of motion to become numerically stiff. Summarising, we see that (57) describes spatial Coulomb friction taking stiction properly into account.

While the force law (57) only describes the Coulomb friction during impulse free motion, we also need a force law for impact impulses $\boldsymbol{\Lambda}_T$. These are found from the exact same form as (57) by replacing $\boldsymbol{\gamma}_T$ with its right limit $\boldsymbol{\gamma}_T^+$ and

inserting $\boldsymbol{\Lambda}_T$ instead of $\boldsymbol{\lambda}_T$ both in (57) and in the convex set C_T in (58).

3) Rolling Friction: The snake robot modeled in this paper has cylindrical links which means that it may roll sideways. The spatial Coulomb friction described in the previous section arises from translational motion. In addition, there is also a force that resists the rolling motion of the snake robot. We model this force as a 'rolling friction' $\boldsymbol{\lambda}_V \in \mathbb{R}^2$ (additional subscripts omitted for simplicity) in this paper by employing the same set-valued force law as for the tangential Coulomb friction force $\boldsymbol{\lambda}_T$ in Section V-B2. However, we consider the rolling friction to be isotropic and therefore we find the rolling friction as

$$-\boldsymbol{\gamma}_V \in N_{C_V}(\boldsymbol{\lambda}_V), \qquad (59)$$

where

$$C_V = \left\{ \boldsymbol{\lambda}_V \mid \|\boldsymbol{\lambda}_V\| \leq \mu_V \lambda_N \right\}, \qquad (60)$$

and $\mu_V > 0$ is the friction coefficient.

The general form of the force law (59) is also valid for impact impulses $\boldsymbol{\Lambda}_V$ in the same way as for the tangential Coulomb friction described in Section V-B2. Subsequently, the impact impulse is found by exchanging $\boldsymbol{\gamma}_V$ with $\boldsymbol{\gamma}_V^+$ and $\boldsymbol{\lambda}_V$ with $\boldsymbol{\Lambda}_V$ in (59)-(60).

4) Constitutive Laws as Projections: An inclusion can not be directly employed in numerical calculations. Hence, we transform the force laws (53), (57), and (59) which have been stated as an inclusion to a normal cone, into an equality. This is achieved through the so-called proximal point function $\text{prox}_C(\boldsymbol{x})$, which equals $\boldsymbol{x}$ if $\boldsymbol{x} \in C$ and equals the closest point in C to $\boldsymbol{x}$ if $\boldsymbol{x} \notin C$. The set C must be convex. Using the proximal point function we transform the force laws into implicit equalities (see [22])

$$-\gamma_\kappa \in N_{C_\kappa}(\lambda_\kappa) \iff \lambda_\kappa = \text{prox}_{C_\kappa}(\lambda_\kappa - r_\kappa \gamma_\kappa), \qquad (61)$$

where $r_\kappa > 0$ for $\kappa = N, T, V$.

C. Joint Actuators

Each cardan joint has 2 DOF that are controlled by two joint actuators. The actuators are modeled as controlled torques applied around the axes of rotation for the joint. Fig. 5 illustrates how the direction of positive rotation is defined. Define for link i a positive control torque τ_{v_i} to give a positive rotational velocity around $\boldsymbol{e}_x^{B_{i+1}}$ and a positive control torque τ_{h_i} to give a positive rotational velocity around $\boldsymbol{e}_y^{B_i}$, both with respect to link i. The total torque $\boldsymbol{\tau}_{C_i} \in \mathbb{R}^3$ applied to link i is

$$\boldsymbol{\tau}_{C_i} = \begin{bmatrix} 0 \\ \tau_{h_i} \\ 0 \end{bmatrix} - \mathbf{R}_{B_{i-1}}^{B_i} \begin{bmatrix} 0 \\ \tau_{h_{(i-1)}} \\ 0 \end{bmatrix} + \mathbf{R}_{B_{i+1}}^{B_i} \begin{bmatrix} \tau_{v_i} \\ 0 \\ 0 \end{bmatrix} - \begin{bmatrix} \tau_{v_{(i-1)}} \\ 0 \\ 0 \end{bmatrix} \qquad (62)$$

for $i = 1, \ldots, n$, where the relative rotation matrix is

$$\mathbf{R}_{B_{i+1}}^{B_i} = \left(\mathbf{R}_{B_i}^I\right)^T \mathbf{R}_{B_{i+1}}^I, \qquad (63)$$

and $\tau_{h_0} = \tau_{v_0} = \tau_{h_n} = \tau_{v_n} = 0$. The vector of the torques applied to all links $\boldsymbol{\tau}_C \in \mathbb{R}^{6n}$ is

$$\boldsymbol{\tau}_C = \begin{bmatrix} \boldsymbol{0}_{1\times3} & \boldsymbol{\tau}_{C_1}^T & \boldsymbol{0}_{1\times3} & \boldsymbol{\tau}_{C_2}^T & \cdots & \boldsymbol{0}_{1\times3} & \boldsymbol{\tau}_{C_n}^T \end{bmatrix}^T. \qquad (64)$$
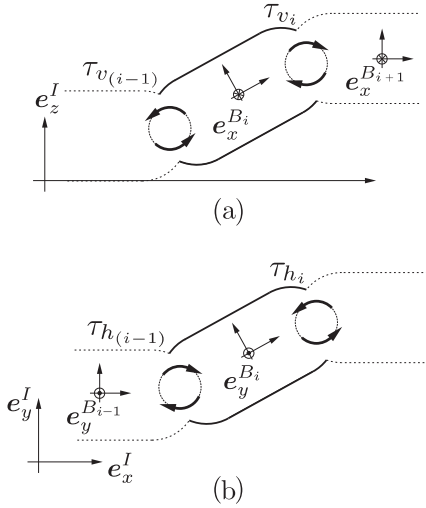
(a)

(b)

Fig. 5.   Control Torques for (a) side-view and (b) top-view.

VI. MOTION PATTERN AND JOINT CONTROL

In this chapter, we will define the joint angles and show how to control them for snake robot locomotion.

A. Accessing and Control of Joint Angles

The joint angles are not directly accessible from the non-minimal coordinates, but can be calculated from the relative rotation matrices $\mathbf{R}_{B_{i+1}}^{B_i}$ in (63). Assume that $\mathbf{R}_{B_{i+1}}^{B_i}$ is constructed from successive rotations (Euler angles with the zyx-convention) α_{z_i}, α_{h_i}, and α_{v_i}: $\mathbf{R}_{B_{i+1}}^{B_i} = \mathbf{R}_{\alpha_{z i}}\mathbf{R}_{\alpha_{h i}}\mathbf{R}_{\alpha_{v i}}$. Since we have cardan joints, let $\mathbf{R}_{\alpha_{z i}} = \mathbf{I}_{3\times 3}$ be the rotation around the $e_z^{B_i}$-axis, and let $\mathbf{R}_{\alpha_{h i}}$ and $\mathbf{R}_{\alpha_{v i}}$ describe the rotation around $e_y^{B_i}$ and $e_x^{B_{i+1}}$, respectively. Hence, α_{h_i} describes the DOF of the cardan joint between link i and link $i + 1$ that moves link i and $i + 1$ from side to side, and α_{v_i} describes the lifting and lowering of the links. The rotation angles can now be found from the relative rotation matrix (63) as

$$\alpha_{v_i} = \tan^{-1}\left[(\mathbf{R}_{B_{i+1}}^{B_i})_{32}/(\mathbf{R}_{B_{i+1}}^{B_i})_{33}\right] \qquad (65)$$

$$\alpha_{h_i} = -\sin^{-1}(\mathbf{R}_{B_{i+1}}^{B_i})_{31}, \qquad (66)$$

for $i = 1, \ldots, n - 1$ where $\left(\mathbf{R}_{B_{i+1}}^{B_i}\right)_{32}$ is the element of the matrix $\mathbf{R}_{B_{i+1}}^{B_i}$ in row 3 column 2, etc.

The rotational velocities of the joints are found directly from the rotational velocities of the links. We define the rotational velocity for sideways motion as $\omega_{h_i} = d_2^T\omega_{J_i}$ and lifting motion as $\omega_{v_i} = d_1^T\omega_{J_i}$ for the joint between link i and $i+1$, where $d_1^T = \begin{bmatrix} 1 & 0 & 0 \end{bmatrix}$, $d_2^T = \begin{bmatrix} 0 & 1 & 0 \end{bmatrix}$, and

$$\omega_{J_i} = {}_{B_{i+1}}\omega_{IB_{i+1}} - \left(\mathbf{R}_{B_{i+1}}^{B_i}\right)^T {}_{B_i}\omega_{IB_i}. \qquad (67)$$

Let the desired values of α_{h_i} and α_{v_i} be $\alpha_{h_i,r}$ and $\alpha_{v_i,r}$, respectively. In addition, the reference values for the joint velocities ω_{h_i}, ω_{v_i} are given by $\dot\alpha_{h_i,r}$ and $\dot\alpha_{v_i,r}$, respectively. Then, PD-controllers for the joints are

$$\tau_{h_i} = K_{h_p}\left(\alpha_{h_i} - \alpha_{h_i,r}\right) + K_{h_d}\left(\omega_{h_i} - \dot\alpha_{h_i,r}\right) \qquad (68)$$

$$\tau_{v_i} = K_{v_p}\left(\alpha_{v_i} - \alpha_{v_i,r}\right) + K_{v_d}\left(\omega_{v_i} - \dot\alpha_{v_i,r}\right), \qquad (69)$$

for $i = 1, \ldots, n - 1$ where K_{h_p}, K_{h_d}, K_{v_p}, and K_{v_d} are positive constants and equal for all i.

B. Motion Pattern and Reference Angles

A general expression for defining some of the most common motion patterns for snake robots is given by

$$\alpha_{h_i,r} = A_h \sin\left(\omega_h t + (i-1)\delta_h\right) + \psi_h \qquad (70)$$

$$\alpha_{v_i,r} = A_v \sin\left(\omega_v t + (i-1)\delta_v + \delta_0\right) + \psi_v, \qquad (71)$$

for $i = 1, \ldots, n - 1$ where $\alpha_{h_i,r}$ and $\alpha_{v_i,r}$ are the reference angles for α_{h_i} and α_{v_i}, and A_h, A_v are the amplitude of oscillation, ω_h, ω_v are the angular frequencies, δ_h, δ_v are the phase offsets, and ψ_h, ψ_v are the angle offsets, for the horizontal and vertical wave, respectively [3]. The offset between the vertical and horizontal wave is given by δ_0.

Two motion patterns that biological snakes use have been employed in this paper. The first motion pattern is called 'lateral undulation' (also denoted 'serpentine crawling') where locomotion is obtained by propagating horizontal waves from the front to the rear of the snake body while exploiting roughness in the terrain and digging its body into the ground. These latter two properties are the motivation for our anisotropic friction model. The second motion pattern is called 'sidewinding' and is mainly used by biological snakes moving on uniform surfaces [30]. Parts of the snake are lying relatively stationary on the ground while the rest of the body is lifted and moved forward resulting in a looping movement during locomotion.

VII. NUMERICAL ALGORITHM - TIME-STEPPING

The numerical solution of the equality of measures is found with an algorithm introduced in [23] (see also [22], [24]) called the time-stepping-method described in the following. The methods applied in Section VII-A and VII-B are based on [27], except for the direct calculation of the bilateral contact impulsions which we have introduced.

A. Time Discretization

Let t_l denote the time at time-step $l = 1, 2, 3, \ldots$ where the step size is $\Delta t = t_{l+1} - t_l$. Consider the (usually very short) time interval $I = [t_A, t_E]$, and let $t_A = t_l$. Define $q_A = q(t_A)$, $u_A = u(t_A)$ which are admissible with respect to both the unilateral and bilateral constraints, and the unit norm constraint on the Euler parameters. Our goal is now to find $q_E = q(t_E)$. We use the states of the system at the *midpoint* $t_M = t_A + \frac{1}{2}\Delta t$ of the time-interval I to decide which contact points are active (i.e. which links are touching the ground). The coordinates (positions and orientations) at t_M are found from

$$q_M = q_A + \frac{\Delta t}{2}\mathbf{F}(q_M)u_A, \qquad (72)$$

where we have used the equality $\dot{\boldsymbol{p}} = \frac{1}{2}\bar{\mathbf{H}}^\mathrm{T}{}_{B_i}\boldsymbol{\omega}_{IB_i}$ [26],

$$\mathbf{F}(\boldsymbol{q}_M) = \begin{bmatrix} \mathbf{F}_{H_1} & \mathbf{0}_{7\times 6} & \cdots & \mathbf{0}_{7\times 6} \\ \mathbf{0}_{7\times 6} & \mathbf{F}_{H_2} & \cdots & \vdots \\ \vdots & & \ddots & \mathbf{0}_{7\times 6} \\ \mathbf{0}_{7\times 6} & \cdots & \mathbf{0}_{7\times 6} & \mathbf{F}_{H_n} \end{bmatrix} \quad (73)$$

$$\mathbf{F}_{H_i} = \begin{bmatrix} \mathbf{I}_{3\times 3} & \mathbf{0}_{3\times 3} \\ \mathbf{0}_{4\times 3} & \frac{1}{2}\bar{\mathbf{H}}_i^\mathrm{T} \end{bmatrix} \in \mathbb{R}^{7\times 6}, \quad (74)$$

and $\bar{\mathbf{H}}_i$ is found from (6) by inserting the orientation of link i at time t_M. The approximation of the matrices $\mathbf{W}_\Xi$, where $\Xi = N, T, J, V$, on the time-interval I is given as $\mathbf{W}_{\Xi M} := \mathbf{W}_\Xi(\boldsymbol{q}_M)$. The same applies for $\boldsymbol{h}_M := \boldsymbol{h}(\boldsymbol{q}_M, \boldsymbol{u}_A)$. A numerical approximation of the equality of measures (46) over the time-interval I can now be written as

$$\mathbf{M}(\boldsymbol{u}_E - \boldsymbol{u}_A) - \boldsymbol{h}_M \Delta t - \boldsymbol{S} - \mathbf{W}_{JM}\boldsymbol{P}_J = \boldsymbol{\tau}_C \Delta t, \quad (75)$$

where

$$\boldsymbol{S} = \sum_{a\in\mathcal{I}} (\mathbf{W}_{NM})_a P_{N_a} + [(\mathbf{W}_{TM})_{2a-1} (\mathbf{W}_{TM})_{2a}]\boldsymbol{P}_{T_a} \\ + \sum_{a\in\mathcal{I}} [(\mathbf{W}_{VM})_{2a-1} (\mathbf{W}_{VM})_{2a}]\boldsymbol{P}_{V_a} \quad (76)$$

and P_{N_a}, $\boldsymbol{P}_{T_a}$, $\boldsymbol{P}_{V_a}$, and $\boldsymbol{P}_J$ are the contact impulsions during the time-interval I. They consist of forces λ acting *during* I, and possible impulses Λ acting *in* the time-interval I. The subscript $_a$ denotes which link the contact impulsions are acting on, and is employed the same way as for the contact impulse measures in (50). To find the positions and orientations $\boldsymbol{q}_E$ at the end of the time-interval, we need to solve (75) for $\boldsymbol{u}_E$ and the contact impulsions. The contact impulsions associated with ground contact are found using the prox-functions described in Section V-B4 for the set of active contact points $\mathcal{I}$. Hence, the constitutive laws (61) for the ground contact impulsions may now be written

$$P_{N_a} = \mathrm{prox}_{C_N}(P_{N_a} - r_N\gamma_{NE_a}), \quad (77)$$
$$\boldsymbol{P}_{T_a} = \mathrm{prox}_{C_T}(\boldsymbol{P}_{T_a} - r_T\boldsymbol{\gamma}_{TE_a}), \quad (78)$$
$$\boldsymbol{P}_{V_a} = \mathrm{prox}_{C_V}(\boldsymbol{P}_{V_a} - r_V\boldsymbol{\gamma}_{VE_a}), \quad (79)$$

where $r_N, r_T, r_V > 0$, $a \in \mathcal{I}$, γ_{NE_a} is the a-th element of the vector $\boldsymbol{\gamma}_{NE}$, and $\boldsymbol{\gamma}_{TE_a}$, $\boldsymbol{\gamma}_{VE_a}$ are the vectors of the $(2a-1)$−th and $2a$-th elements of $\boldsymbol{\gamma}_{TE}$ and $\boldsymbol{\gamma}_{VE}$, respectively, and

$$\boldsymbol{\gamma}_{NE} := \boldsymbol{\gamma}_N(\boldsymbol{q}_M, \boldsymbol{u}_E) = \mathbf{W}_{NM}^\mathrm{T}\boldsymbol{u}_E, \quad (80)$$
$$\boldsymbol{\gamma}_{TE} := \boldsymbol{\gamma}_T(\boldsymbol{q}_M, \boldsymbol{u}_E) = \mathbf{W}_{TM}^\mathrm{T}\boldsymbol{u}_E, \quad (81)$$
$$\boldsymbol{\gamma}_{VE} := \boldsymbol{\gamma}_V(\boldsymbol{q}_M, \boldsymbol{u}_E) = \mathbf{W}_{VM}^\mathrm{T}\boldsymbol{u}_E. \quad (82)$$

The constitutive laws (77)-(82) are valid for completely inelastic impact.

The constraints on the joints are bilateral and it therefore holds that $\boldsymbol{\gamma}_{JE} := \boldsymbol{\gamma}_J(\boldsymbol{q}_E, \boldsymbol{u}_E) = \mathbf{W}_{JM}^\mathrm{T}\boldsymbol{u}_E = \mathbf{0}\,\forall t$. This allows us to directly compute the associated contact impulsions $\boldsymbol{P}_J$ by solving (75) for $\boldsymbol{P}_J$ with $\boldsymbol{u}_E = \mathbf{0}$. By solving for $\boldsymbol{P}_J$ and solving (75)-(81), we find that

$$\boldsymbol{q}_E = \boldsymbol{q}_M + \frac{\Delta t}{2}\mathbf{F}(\boldsymbol{q}_M)\boldsymbol{u}_E. \quad (83)$$

B. Solving for the Contact Impulsions

In this section, we show how to calculate the contact impulsions P_{N_a}, $\boldsymbol{P}_{T_a}$, $\boldsymbol{P}_{V_a}$, and $\boldsymbol{P}_J$ in (76) for $a \in \mathcal{I}$. The numerical integration algorithm used in this paper is called a time-stepping method which allows for a simultaneous treatment of both impulsive and non-impulsive forces during a time-step. The frictional contact problem, defined by (75)-(82) and finding $\boldsymbol{P}_J$, needs to be solved for each time-step t_l. A Modified Newton Algorithm [31] has been chosen to solve the nonlinear problem iteratively because of its simplicity. Let the superscript $^{(k)}$ denote the current iteration of the Modified Newton Algorithm, and initialize all contact impulsions (for active contacts) with the value they had the last time their corresponding contact point was active. Let those that *were* active be initialized with their previous values. Now, the algorithm may be written as

1) Solve

$$\boldsymbol{P}_J^{(k)} = (\mathbf{W}_{JM}^\mathrm{T}\mathbf{M}^{-1}\mathbf{W}_{JM}^\mathrm{T})^{-1} \quad (84)$$
$$\cdot [\mathbf{W}_{JM}^\mathrm{T}\boldsymbol{u}_A - \mathbf{W}_{JM}^\mathrm{T}\mathbf{M}^{-1}(\boldsymbol{h}_M\Delta t + \boldsymbol{S}^{(k)} + \boldsymbol{\tau}_C\Delta t)]$$

where

$$\boldsymbol{S}^{(k)} = \sum_{a\in\mathcal{I}}(\mathbf{W}_{NM})_a P_{N_a}^{(k)} \\ + \sum_{a\in\mathcal{I}}[(\mathbf{W}_{TM})_{2a-1} (\mathbf{W}_{TM})_{2a}]\boldsymbol{P}_{T_a}^{(k)} \\ + \sum_{a\in\mathcal{I}}[(\mathbf{W}_{VM})_{2a-1} (\mathbf{W}_{VM})_{2a}]\boldsymbol{P}_{V_a}^{(k)}. \quad (85)$$

2) Solve $\boldsymbol{u}_E^{(k+1)}$ from

$$\mathbf{M}(\boldsymbol{u}_E^{(k+1)} - \boldsymbol{u}_A) - \boldsymbol{h}_M\Delta t - \boldsymbol{S}^{(k)} - \mathbf{W}_{JM}\boldsymbol{P}_J^{(k)} = \boldsymbol{\tau}_C\Delta t \quad (86)$$

3) Solve for $a \in \mathcal{I}$

$$P_{N_a}^{(k+1)} = \mathrm{prox}_{C_N}(P_{N_a}^{(k)} - r_N\gamma_{NE_a}^{(k+1)}), \quad (87)$$
$$\boldsymbol{P}_{T_a}^{(k+1)} = \mathrm{prox}_{C_T}(\boldsymbol{P}_{T_a}^{(k)} - r_T\boldsymbol{\gamma}_{TE_a}^{(k+1)}), \quad (88)$$
$$\boldsymbol{P}_{V_a}^{(k+1)} = \mathrm{prox}_{C_V}(\boldsymbol{P}_{V_a}^{(k)} - r_V\boldsymbol{\gamma}_{VE_a}^{(k+1)}), \quad (89)$$

where

$$\boldsymbol{\gamma}_{NE}^{(k+1)} = \mathbf{W}_{NM}^\mathrm{T}\boldsymbol{u}_E^{(k+1)}, \quad (90)$$
$$\boldsymbol{\gamma}_{TE}^{(k+1)} = \mathbf{W}_{TM}^\mathrm{T}\boldsymbol{u}_E^{(k+1)}, \quad (91)$$
$$\boldsymbol{\gamma}_{VE}^{(k+1)} = \mathbf{W}_{VM}^\mathrm{T}\boldsymbol{u}_E^{(k+1)}. \quad (92)$$

Repeat steps 1. to 3. until

$$\|\boldsymbol{P}_N^{(k+1)} - \boldsymbol{P}_N^{(k)}\| + \|\boldsymbol{P}_T^{(k+1)} - \boldsymbol{P}_T^{(k)}\| \\ + \|\boldsymbol{P}_V^{(k+1)} - \boldsymbol{P}_V^{(k)}\| < \epsilon, \quad (93)$$

where $\epsilon > 0$ is a user-defined tolerance. Subsequently, $\boldsymbol{q}_E$ is calculated from (83) and the calculation of the time-step is finished. Usually, a higher value of the parameters r_N, r_T, r_V yields a faster convergence rate at the risk of divergence. However, a general convergence result for the Modified Newton Algorithm does not exist. The constitutive laws (87)-(92) used to describe the contact impulses are given

on *velocity level*. This means that the bilateral constraints on position level, and the unit norm constraint on the Euler parameters are in general not satisfied. A solution to these problems is suggested in the following.

C. Constraint Violation

After the Modified Newton Algorithm has converged and q_E has been found from (83), the unit-norm constraint $\|p_i\| = 1$ is satisfied from $p_{E_i}^{new} = p_{E_i}/\|p_{E_i}\|$ for $i = 1, \ldots, n$ where p_{E_i} is the quaternion describing the orientation of link i. The new quaternions should now be inserted into q_E.

The links have to be projected so that the bilateral constraints (12), (13) are satisfied. This is done in a two-step process while keeping the position and orientation of link 1 fixed. First, the orientation of the positions of the remaining links are altered so that $g_{J_{i\phi}} = 0$ is satisfied for $i = 1, \ldots, n-1$. In this process, all the $e_z^{B_i}$-axes are kept fixed, while the $e_x^{B_i}$ and $e_y^{B_i}$ are changed if necessary. Subsequently, the remaining links are translated so that $g_{J_{i\chi}} = 0$ is satisfied for $i = 1, \ldots, n-1$, $\chi = x, y, z$. The new positions of the links should now be inserted into q_E. Now, the positions q_E and velocities u_E can be used as the initial states for the next time-step t_{l+1}.

VIII. SIMULATIONS AND EXPERIMENTAL VALIDATION

In this section, we present simulations of the mathematical model together with experiments with a real snake robot. First, we present the model and simulation parameters. Second, simulation results of the motion pattern lateral undulation are given with orthotropic friction. Finally, the latter three sections present the experimental setup together with simulation and experimental results of the motion patterns lateral undulation and sidewinding with isotropic friction.

A. Model and Simulation Parameters

The snake robot Aiko in Fig. 1 was used as a basis for the parameters in the mathematical model. The model parameters are for $i = 1, \ldots, n$: Aiko has $n = 11$ links. The length $L_i = 0.122$ m and radius $L_{SC_i} = 0.0525$ m of each link is found by measuring one of the links used on Aiko. Moreover, Aiko weighs 7.5 kg and we therefore assume that each link weighs $m_i = 7.5/11 \text{kg} \approx 0.682$ kg since all links are approximately equal. The distance from the centre of gravity of a link to the centre of the spheres used for contact with the ground in the model is calculated to be $L_{GS_i} = 0.0393$ m by assuming a 45 degree maximum joint deflection and that the cylindrical parts of the model should not come into each other for a maximum joint angle. The moments of inertia $\Theta_{1i} = 9.63 \times 10^{-4}$ kg m^2, $\Theta_{3i} = 2.35 \times 10^{-4}$ kg m^2 are calculated by assuming each link to be a cylinder of length L_i and radius L_{SC_i} with a uniform mass distribution.

The controller parameters are $K_{h_p} = 40$ Nm, $K_{h_d} = 0.2$ Nm·s, $K_{v_p} = 800$ Nm, and $K_{v_d} = 0.2$ Nm·s. The acceleration of gravity is $g = 9.81$ m/s^2. The simulation parameters are as follows: $r_N = 0.1$, $r_T = 0.01$, $r_V = 0.05$, $t_{\text{start}} = 0$ s, $t_{\text{stop}} = 15$ s, $\Delta t = \frac{t_{\text{stop}} - t_{\text{start}}}{N}$ s, and $N = 4000(t_{\text{stop}} - t_{\text{start}})$. The Coulomb friction coefficients are
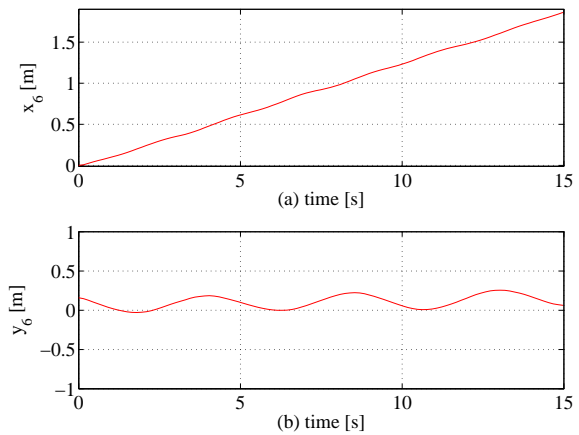

Fig. 6. Simulation results (solid line) of the position (x_6, y_6) of the centre of gravity of link 6 in the (e_x^I, e_y^I)-plane during lateral undulation. The model is simulated with orthotropic friction.

given together with the presentation of the simulations since we have not employed the same friction coefficients for all simulations.

B. Lateral Undulation: Simulation Results

In this section, we let the snake robot move by the motion pattern lateral undulation (see Section VI). We include this motion pattern since it is commonly used for snake robots (see e.g. [1], [10], [12], [13], [32]–[34]) and we therefore want to show that the desired (forward) motion is obtained for our model. We do not provide an experimental validation in this section since our snake robot Aiko does not have the orthotropic friction property necessary for efficient locomotion by lateral undulation on a flat surface. However, we compare simulation and experimental results for lateral undulation with *isotropic* friction in Section VIII-D.

The Coulomb friction coefficients $\mu_{T_x} = 0.1$ (along the snake robot body) and $\mu_{T_y} = 0.5$ (transversal to the body) are employed for the simulation of lateral undulation in this section. Hence, orthotropic friction is obtained. The motion pattern is implemented using the joint reference angles given by (70)-(71) with the parameters $A_h = 30\pi/180$ rad, $\omega_h = 80\pi/180$ rad/s, $\delta_h = -50\pi/180$ rad, $A_v = \delta_v = \psi_v = \psi_h = \delta_0 = 0$ rad, and $\omega_v = 0$ rad/s. We let the snake robot start in a curved posture with its centre line approximately along the e_x^I-axis and with its initial joint angles given by $\alpha_{h_i}(0)$ and $\alpha_{v_i}(0)$, respectively.

Fig. 6 shows the position of the centre of gravity of the middle link ($i = 6$) of the snake robot. We see that the snake robot behaves as expected: The snake robot starts moving steadily forward mainly along the e_x^I-axis. The forward motion would not have been the result for an isotropic friction model (i.e. $\mu_{T_x} = \mu_{T_y}$). In that case, the snake robot would have moved slowly backward as we will see in Section VIII-D. In order to increase the velocity of a snake robot, even with isotropic friction, the snake robot may push against external objects to move forward. Such an approach is elaborated on in e.g. [35], [36].

C. The Experimental Setup

The snake robot Aiko (Fig. 1) used in the experiments was built in 2006 at the NTNU/SINTEF Advanced Robotics Laboratory[1] in Trondheim, Norway. Aiko has ten 2 DOF cardan joints and 11 links. The length L_i and mass m_i of the links are the same as given for the mathematical model in Section VIII-A. The metal sphere used as a 'face' in Fig. 1 was removed in the experiments to obtain a uniform weight distribution along the snake robot. The friction coefficients in the model were calculated from the measurements obtained by dragging Aiko from a scale along the particle board. The friction coefficients were found to be $\mu_{T_x} = \mu_{T_y} = 0.2$ and these values will be employed in the simulations in the remainder of this paper.

Each 2 DOF cardan joint was actuated by two 6 W DC-motors. The two motors were controlled by a controller with dynamic feedback (see [37]) implemented on an Atmel ATmega128 microcontroller. The snake robot joint reference angles were sent with a frequency of 10 Hz from a PC, via a CAN-bus to the microcontrollers. The position of the centre of the middle link (link 6) was tracked using a Vicon MX Motion Capture System with 4 cameras (MX3) together with Matlab Simulink. The Vicon programme (Vicon iQ 2.0) ran on a computer with 4 Intel Xeon 3 GHz processors and 2 GB RAM. The logging of motion data was synchronized in time through a TCP-connection between the PC that controlled Aiko and the Vicon-computer at the start-up of the transmission of the desired snake robot joint angles. Data logging was performed at 20 Hz. We have chosen to let the position of link 6 represent the position of the snake robot, because then we filter any transient behaviour of the snake robot that might occur at its ends and it is thus easier to focus on the general motion of the snake robot. The centre of gravity of the whole snake robot (instead of a specific link) can also be advantageous to be used to represent the position of the snake robot. However, such an approach is cumbersome to realize with our Vicon system.

Particle boards were used as the ground surface.

D. Lateral Undulation: Simulation and Experimental results

In this section, we compare simulation and experimental results for lateral undulation with isotropic friction. The reference joint angles are calculated from (70)-(71) with the parameters $A_h = 40\pi/180$ rad, $\omega_h = 80\pi/180$ rad/s, $\delta_h = -50\pi/180$ rad, $A_v = \delta_v = \delta_0 = 0$ rad, $\omega_v = 0$ rad/s, and $\psi_h = \psi_v = 0$, for both the simulation and the experiment. We let the snake robot start in a curved posture with its centre line approximately along the e_x^I-axis and with its initial joint angles given by $\alpha_{h_i}(0)$ and $\alpha_{v_i}(0)$. Fig. 7 shows both the position of link 6 calculated from the mathematical model in the simulation and the position logged from the experiment with Aiko. We see that the snake robot moves slowly backward along the e_x^I-axis. From Fig. 7 we see that the 3D model display the same trend in motion as observed in the experiment. However, the distance travelled is greater in simulation and we have tried varying the friction coefficients

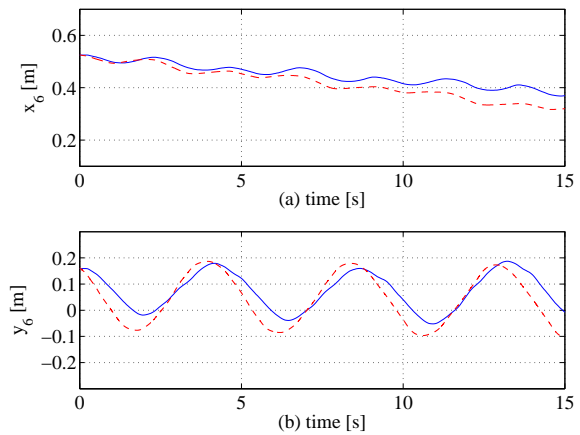[1]http://www.sintef.com/snakerobots

Fig. 7. Position of link 6 during lateral undulation with isotropic friction on a flat plane: simulation (dashed line) and experimental (solid line) results.

(while still keeping isotropic friction), but this did not seem to have a noticeable effect on the simulation results. The difference in distance travelled may come as a consequence of that the model of the snake robot is able to control its joints more accurately and thus is able to reach the maximum amplitude when it is required to do so. Also, this suggests that the friction contact between the snake robot and the ground surface is even more complex than what has been accounted for in the model. A more elaborate list of possible sources of errors is given in Section VIII-F.

We note from these simulation and experimental results that the direction of locomotion by lateral undulation with isotropic friction is the same as the direction of the waves that is propagated along the body of the snake robot. This is coherent with results found in [38] where this phenomenon is elaborated on.

E. Sidewinding: Simulation and Experimental Results

In this section, we present and compare the simulation results and the experimental results for the motion pattern sidewinding. The joint reference angles are found from (70)-(71) with the parameters $A_h = 30\pi/180$, $\omega_h = 80\pi/180\frac{1}{s}$, $\delta_h = -50\pi/180$, $A_v = 10\pi/180$, $\omega_v = \omega_h$, $\delta_v = \delta_h$, $\delta_0 = 90\pi/180$, and $\psi_h = \psi_v = 0$, for both the simulation and the experiment. We employ a 'soft start' approach during start-up of the snake robot from its initial (straight) posture to avoid large steps in the reference signal. To this end, we override the expressions (70)-(71) and set $\alpha_{h_i}(t) = 0$ rad until the reference signal is within $|\alpha_{h_i}(t)| \leq 3\pi/180$ rad for the first time after start-up. The same applies for α_{v_i}. The shape of the snake robot during start-up with the 'soft-start' approach is illustrated in Fig. 8 for sidewinding.

Fig. 9 illustrates how Aiko and the model move during the 15 second simulation of sidewinding locomotion. Since all the simulations have now been performed, a note on the computational cost is appropriate. All simulations were performed on a Pentium-M 1.8 GHz computer running Matlab R2006a. For 20 seconds simulations it took on average about 7.1 minutes to simulate 1 second of sidewinding motion and only 1.3 minutes
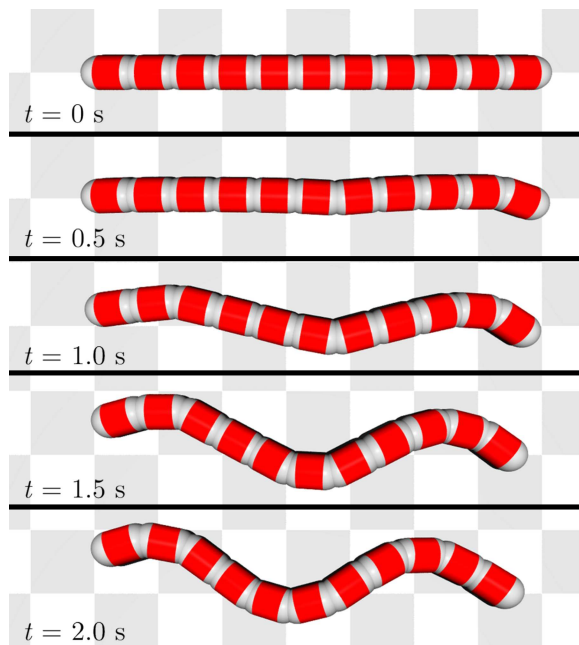
Fig. 8. Top-down view of snake robot postures during simulation of start-up with the 'soft-start' approach for sidewinding.
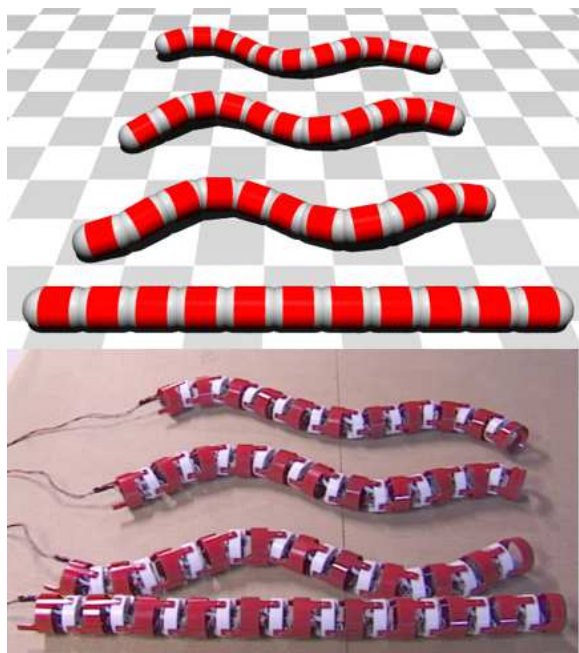

Fig. 9. Aiko (bottom) and simulated snake robot (top) during sidewinding. The images show the snake robot at $t = 0$ s (straight posture), $t = 5$ s, $t = 10$ s, and $t = 15$ s.

to simulate 1 second of lateral undulation. The difference in simulation speed arises from that the 3D motion during sidewinding is more complex than planar motion by lateral undulation. The simulation speed can be greatly increased by instead implementing the model in for example C++. However, we have chosen to first implement the model in Matlab in order to keep the time it takes to implement the model relatively short.

Fig. 10 and Fig. 11 display the position of link 6 for the 3D model and Aiko during sidewinding. We observe from the figures that the model almost follows the $\boldsymbol{e}_y^I$-axis, while Aiko steadily turns somewhat to the right. In addition, the model covers a greater distance than Aiko. We see from Fig. 10 and Fig. 11 (b) that the simulation results have the same trend and approximate frequency as the experimental results along the $\boldsymbol{e}_y^I$-axis. The variance in trend is more noticeable along the $\boldsymbol{e}_x^I$-axis due to the turning motion of Aiko. Moreover, a slight initial difference between the orientation of Aiko and the model may contribute to the discrepancy in heading. We discuss in Section VIII-F various reasons for the differences between the simulation and experimental results. For sidewinding, we believe that one of the most important differences between the 3D model and Aiko is that Aiko is not able to control its joints accurately. This is particularly the case for vertical (lifting) motion which is needed for sidewinding. By inspecting Aiko closely during the experiment, we noticed that a large part of its body was touching the ground at the same time. This was not the case in the simulation where the snake robot joints were accurately controlled which resulted in that most if its body was lifted from the ground during locomotion.

We observe from Fig. 10 and Fig. 11 (b) that Aiko sometimes slides a little backward (at $t \approx 5$ s, $t \approx 9$ s and $t \approx 14$ s). We have tried to reproduce this phenomenon in the 3D model by lowering and increasing the friction coefficient. We have also tried a variety of anisotropic friction properties, but without any luck. The backward motion might be a result of Aiko not being able to lift its links properly. The links that are supposed to be lifted and moved forward are instead sometimes dragged along the particle board. This results in a friction force which acts in the opposite direction of the desired motion of the snake robot. This friction force might result in that some of the parts that are supposed to be lying stationary on the ground are instead pushed slightly backward.
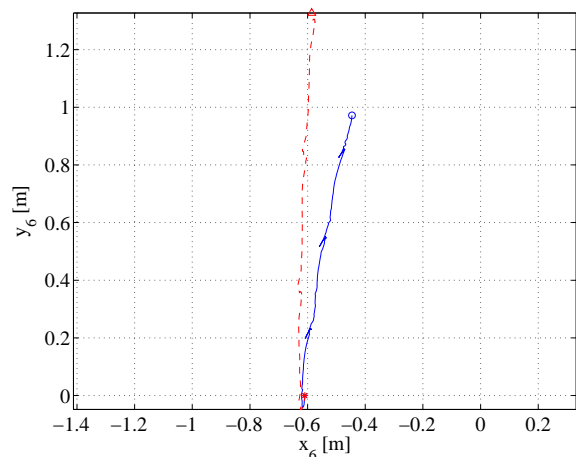

Fig. 10. Position of link 6 during sidewinding on a flat plane: simulation (dashed line) and experimental (solid line) results. The triangle and the circle mark the end of the paths.
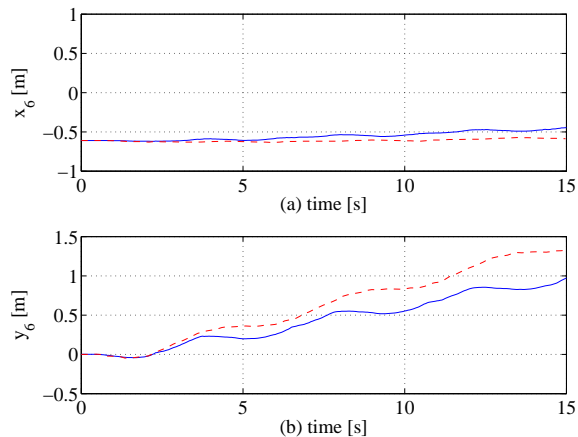
Fig. 11. Position of link 6 during sidewinding on a flat plane: simulation (dashed line) and experimental (solid line) results.

F. Discussion of the Experimental Validation

We see from Fig. 10 and Fig. 11 that the simulation and experimental results compare fairly well. However, the differences between the two results need to be addressed and we list the most important possible sources of errors in the following. These effects have not been included in the mathematical model.

1) Aiko has a noticeable free play in the joints of about $3-5$ degrees. This results in that the control of the joint angles is not completely accurate and a joint angle might not be able to reach its desired angle.

2) The dynamics of the actuators are not modelled. Hence, the actuators in the models are extremely strong and fast, and we are able to accurately control the actual angle of each joint to its desired position. This is not the case for Aiko where the joint motors sometimes saturate and are unable to track the desired joint movement precisely. This particularly the case for vertical motion where larger joint torques are required.

3) The exoskeleton of Aiko is not modelled precisely since this would require a great deal of consideration of the geometry of the snake robot and this would severely complicate the expressions for contact with the environment.

4) For each cardan joint, there is in fact a 2.2 cm distance between the rotational axes for the yaw and pitch motion. However, to simplify the kinematics, we have assumed that the axes intersect.

5) The Stribeck effect (see e.g. [22]) is not included in the model of friction. The Stribeck effect states, roughly speaking, that friction forces acting on a body is reduced just after it is set in motion.

6) The varnish on the underside of the snake robot has been worn down. This has resulted in that the snake robot links slide easier when rolled slightly to one of the sides where the varnish is still present.

7) There was a time-delay between the start-up of the snake robot and the start-up of the logging of position data. This delay ranged between 50 and 150 ms.

8) The physical parameters of the snake robot may be slightly incorrect, partly since we assume that each link has a

uniform mass distribution.

The list of possible errors is long and it is difficult to determine what issues are the most important in order to explain the differences between the simulation and experimental results. Also, the main factors may vary depending on which motion pattern is tested. To this end, we believe that for lateral undulation 1) and 2) are the most important reasons for the differences since the snake robot is always lying flat on the ground. Moreover, for sidewinding locomotion, 1) - 5) affect the comparison the most.

Even though there are several sources of error, we see from the plots that compare the simulation and experimental results that the model gives a satisfactory qualitative description of the snake robot dynamics. The model is not accurate enough to precisely predict the quantitative motion of the snake robot, but it should be possible to improve the accuracy of the model by taking into account the various sources of errors listed above. However, at its current state the model gives a clear indication of how the snake robot will move during sidewinding and lateral undulation with isotropic friction and extending the model will require a considerable amount of work in tailoring the model to the specific snake robot Aiko. Hence, the process will have to be repeated for new snake robot designs. Instead of presenting a model with such a very close resemblance to Aiko, we present a model for synthesis and testing of new 3D motion patterns. Moreover, the comparisons between the simulation and experimental results suggest that our model is valid for this purpose.

IX. CONCLUSIONS AND FURTHER WORK

In this paper, we present a 3D non-smooth mathematical model that enables synthesis and testing of 3D snake robot motion patterns. Experiments show that the models describe in a realistic manner how a real snake robot will behave during locomotion.

The model of the snake robot is developed based on the framework of non-smooth dynamics and convex analysis. This framework allows us to easily incorporate the contact forces with the ground, together with an accurate description of the spatial Coulomb friction. In addition, even though we employ a hybrid model, there is no need for an explicit switch between system equations (when for example an impact occurs) since both the non-impulsive forces and the impact impulses are covered by the same force law together with that we use the time-stepping method for numerical treatment. The use of non-minimal absolute coordinates results in a constant and diagonal mass matrix and an effective way of writing the system equations. Such a constant mass matrix is beneficial in the numerical treatment since it needs only to be inverted once and not in each time-step during simulation.

Simulations of the snake robot during the serpentine motion pattern lateral undulation is performed. The simulation result shows that the orthotropic friction model based on Coulomb's law of dry friction is reasonable since the snake robot moves forward.

Experiments are performed with the snake robot Aiko in Fig. 1 for the serpentine motion patterns lateral undulation and

sidewinding with isotropic friction. Back-to-back comparisons between simulation results and experimental results with these motion patterns are given to validate the mathematical model. The simulation and experimental results compare satisfactory.

The simulation results together with the experimental validation show that the mathematical model presented in this paper gives a satisfactory description of how our snake robot moves in the real world. The model cannot be employed directly (as e.g. a state estimator) to predict the exact motion of our snake robot. However, the comparisons with experimental results show that the model is suitable for developing and testing motion patterns in order to see how a real snake robot will move for a given motion pattern.

We show in this paper how to develop a 3D mathematical model of a snake robot on a flat ground surface. Further work will consist of extending the model to include other ground shapes such as stairs. Also, the model will be used to develop and test new 3D motion patterns for snake robots. Moreover, optimization of non-smooth systems is a growing field of research and the 3D model presented in this paper may one day be employed to optimize gaits with respect to, for example, speed or energy efficiency.

It is hoped that this paper can inspire other communities working on robot manipulators to try out the powerful modeling techniques available in the framework of non-smooth dynamics and convex analysis.

REFERENCES

[1] S. Hirose, *Biologically Inspired Robots: Snake-Like Locomotors and Manipulators*. Oxford: Oxford University Press, 1993.

[2] S. Hirose and A. Morishima, "Design and control of a mobil robot with an articulated body," *Int. J. Rob. Res.*, vol. 9, no. 2, pp. 99–114, 1990.

[3] P. Liljebäck, Ø. Stavdahl, and K. Y. Pettersen, "Modular pneumatic snake robot: 3D modelling, implementation and control," in *Proc. 16th IFAC World Congress*, July 2005.

[4] M. Mori and S. Hirose, "Three-dimensional serpentine motion and lateral rolling by active cord mechanism ACM-R3," in *Proc. IEEE/RSJ Int. Conf. Intelligent Robots and Systems*, 2002, pp. 829–834.

[5] G. Chirikjian and J. Burdick, "Design and experiments with a 30 DOF robot," in *Proc. IEEE Int. Conf. Robotics and Automation*, vol. 3, 1993, pp. 113–119.

[6] ——, "The kinematics of hyper-redundant robot locomotion," *IEEE Trans. Robot. Autom.*, vol. 11, no. 6, pp. 781–793, December 1995.

[7] S. Ma, Y. Ohmameuda, K. Inoue, and B. Li, "Control of a 3-dimensional snake-like robot," in *Proc. IEEE Int. Conf. Robotics and Automation*, vol. 2, Taipei, Taiwan, September 2003, pp. 2067 – 2072.

[8] J. Burdick, J. Radford, and G. Chirikjian, "A 'sidewinding' locomotion gait for hyper-redundant robots," in *Proc. IEEE Int. Conf. Robotics and Automation*, May 1993, pp. 101–106.

[9] A. A. Transeth and K. Y. Pettersen, "Developments in snake robot modeling and locomotion," in *Proc. IEEE Int. Conf. Control, Automation, Robotics and Vision*, Singapore, Dec 2006, pp. 1393–1400.

[10] S. Ma, N. Tadokoro, B. Li, and K. Inoue, "Analysis of creeping locomotion of a snake robot on a slope," in *Proc. IEEE Int. Conf. Robotics and Automation*, September 2003, pp. 2073–2078.

[11] K. McIsaac and J. Ostrowski, "Motion planning for anguilliform locomotion," *IEEE Trans. Robot. Autom.*, vol. 19, no. 4, pp. 637–625, August 2003.

[12] M. Saito, M. Fukaya, and T. Iwasaki, "Serpentine locomotion with robotic snakes," *IEEE Contr. Syst. Mag.*, vol. 22, no. 1, pp. 64–81, February 2002.

[13] S. Ma, "Analysis of creeping locomotion of a snake-like robot," *Adv. Robotics*, vol. 15, no. 2, pp. 205–224, 2001.

[14] I. Tanev, T. Ray, and A. Buller, "Automated evolutionary design, robustness, and adaptation of sidewinding locomotion of a simulated snake-like robot," *IEEE Trans. Robot.*, vol. 21, no. 4, pp. 632–645, August 2005.

[15] P. Lamon, T. Thueer, R. Jordi, and R. Siegwart, "Modeling and optimization of wheeled rovers," in *Proc. 8th ESA Workshop on Advanced Space Technologies for Robotics*, 2004.

[16] S. Ma, Y. Ohmameuda, and K. Inoue, "Dynamic analysis of 3-dimensional snake robots," in *Proc. IEEE/RSJ Int. Conf. Intelligent Robots and Systems*, 2004, pp. 767–772.

[17] F. Matsuno and H. Sato, "Trajectory tracking control of snake robots based on dynamic model," in *Proc. IEEE Int. Conf. on Robotics and Automation*, 2005, pp. 3029–3034.

[18] P. Prautsch, T. Mita, and T. Iwasaki, "Analysis and control of a gait of snake robot," *Trans. IEE J. Ind. Appl. Soc.*, vol. 120-D, pp. 372–381, 2000, mer utfyllende versjon av "Control and Analysis of the Gait of Snake Robots" (Prautsch1999).

[19] B. Brogliato, *Nonsmooth Mechanics*, 2nd ed. London: Springer, 1999.

[20] R. Smith, "Open Dynamics Engine v0.5 user guide," http://ode.org/ode-latest-userguide.html, online. Accessed 15 Nov 2007.

[21] Ch.. Glocker, *Set-Valued Force Laws, Dynamics of Non-Smooth Systems*, ser. Lecture Notes in Applied Mechanics. Berlin: Springer-Verlag, 2001, vol. 1.

[22] R. I. Leine and H. Nijmeijer, *Dynamics and Bifurcations of Non-Smooth Mechanical Systems*, ser. Lecture Notes in Applied and Computational Mechanics. Berlin: Springer Verlag, 2004, vol. 18.

[23] J. J. Moreau, "Unilateral contact and dry friction in finite freedom dynamics," in *Non-Smooth Mechanics and Applications*, ser. CISM Courses and Lectures, J. J. Moreau and P. D. Panagiotopoulos, Eds. Wien: Springer Verlag, 1988, vol. 302, pp. 1–82.

[24] Ch.. Glocker and C. Studer, "Formulation and preparation for numerical evaluation of linear complementarity systems in dynamics," *Multibody System Dynamics*, vol. 13, pp. 447–463, 2005.

[25] A. A. Transeth, R. I. Leine, Ch.. Glocker, and K. Y. Pettersen, "Non-smooth 3D modeling of a snake robot with frictional unilateral constraints," in *Proc. IEEE Int. Conf. Robotics and Biomimetics*, Kunming, China, Dec 2006, pp. 1181–1188.

[26] O. Egeland and J. T. Gravdahl, *Modeling and Simulation for Automatic Control*. Trondheim, Norway: Marine Cybernetics, 2002.

[27] C. Le Saux, R. I. Leine, and Ch.. Glocker, "Dynamics of a rolling disk in the presence of dry friction," *Journal of Nonlinear Science*, vol. 15, no. 1, pp. 27–61, 2005.

[28] R. T. Rockafellar, *Convex Analysis*, ser. Princeton Landmarks in Mathematics. Princeton, New Jersey: Princeton University Press, 1970.

[29] A. A. Transeth, R. I. Leine, Ch.. Glocker, and K. Y. Pettersen, "Non-smooth 3D modeling of a snake robot with external obstacles," in *Proc. IEEE Int. Conf. Robotics and Biomimetics*, Kunminga, China, Dec 2006, pp. 1189–1196.

[30] J. Gray, "The mechanism of locomotion in snakes," *J. Exp. Biol.*, vol. 23, no. 2, pp. 101–120, 1946.

[31] P. Alart and A. Curnier, "A mixed formulation for frictional contact problems prone to Newton like solution methods," *Comput. Method. Appl. M.*, vol. 92, pp. 353–375, 1991.

[32] J. Ostrowski and J. Burdick, "Gait kinematics for a serpentine robot," in *Proc. IEEE Int. Conf. Robotics and Automation*, vol. 2, April 1996, pp. 1294–1299.

[33] P. Wiriyacharoensunthorn and S. Laowattana, "Analysis and design of a multi-link mobile robot (serpentine)," in *Proc. IEEE Int. Conf. Robotics, Intelligent Systems and Signal Processing*, vol. 2, December 2002, pp. 694–699.

[34] C. Ye, S. Ma, B. Li, and Y. Wang, "Turning and side motion of snake-like robot," in *Proc. IEEE Int. Conf. Robotics and Automation*, vol. 5, 2004, pp. 5075–5080.

[35] Z. Y. Bayraktaroglu, A. Kilicarslan, A. Kuzucu, V. Hugel, and P. Blazevic, "Design and control of biologically inspired wheel-less snake-like robot," in *Proc. IEEE/RAS-EMBS Int. Conf. Biomedical Robotics and Biomechatronics*, February 2006, pp. 1001–1006.

[36] A. A. Transeth, R. I. Leine, C. Glocker, K. Y. Pettersen, and P. Liljebck, "Snake robot obstacle aided locomotion: Modeling, simulations, and experiments," *IEEE Trans. Robot.*, 2007, to appear.

[37] O. Egeland, *Servo Engineering*. Tapir Forlag, 1993, in Norwegian.

[38] M. Nilsson, "Serpentine locomotion on surfaces with uniform friction," in *Proc. IEEE/RSJ Int. Conf. Intelligent Robots and Systems*, 2004, pp. 1751–1755.

Aksel A. Transeth Aksel Andreas Transeth received his MSc degree and PhD degree in 2004 and 2008, respectively, from the Department of Engineering Cybernetics at the Norwegian University of Science and Technology (NTNU), Trondheim, Norway. He is currently employed as a research scientist by the Norwegian research organization SINTEF at the Department of Applied Cybernetics. His research interests include modeling and control of dynamical systems, biologically inspired locomotion, and robotics.

Remco I. Leine Remco Leine is currently Privatdozent of Mechanics at the ETH Zurich. He received his MSc degree in Mechanical Engineering from the Technical University in Delft in 1996, and received his PhD under the guidance of Professor D. van Campen at the Technical University Eindhoven in 2000. In the following years, he visited the Technical University Munich (Professor F. Pfeiffer), the INRIA Rhône-Alpes (Professor B. Brogliato) and the ETH Zurich (Prof. Ch. Glocker) as a postdoctoral researcher. Since 2003, he is active as Senior Lecturer in the Institute of Mechanical Systems, ETH Zurich. In 2007 he obtained his Habilitation and was appointed as 'Privatdozent'.

His research interests are on the intersection of Non-smooth Dynamics and Nonlinear Dynamics: stability theory for non-smooth systems, friction induced vibration and nonlinear phenomena, discontinuous bifurcations in non-smooth dynamical systems, multibody systems with impact and friction.

Christoph Glocker Christoph Glocker is currently Full Professor of Mechanics at ETH Zurich. He received the Diploma and Doctoral degree in mechanical engineering from Technische Universität München in 1989 and 1995, respectively. In 1996 he has been granted with a Feodor Lynen Fellowship supported by the Alexander von Humboldt Foundation and spent one year at Aristotle University of Thessaloniki. After this stay, he returned in 1997 to TU München as a senior engineer to obtain in 2001 the Certificate of Habilitation in Mechanics by a postdoctoral thesis devoted to non-smooth dynamics, and to move to ETH Zurich afterwards.

A central point in his research is non-smooth dynamics of mechanical systems with finite degrees of freedom which includes, for example, the friction and impact problem in multibody systems, providing a generalization of classical analytical mechanics. He is interested in both, theoretical and practical questions concerning the mechanical modeling, the mathematical formulation, and the numerical treatment of systems with discontinuities, as well as their applications to industrial problems.

Kristin Y. Pettersen Kristin Ytterstad Pettersen received her MSc and PhD degrees in Electrical Engineering at the Norwegian University of Science and Technology (NTNU), Trondheim, Norway, in 1992 and 1996 respectively. She became Associate Professor in 1996 and in 2002 Professor at the Department of Engineering Cybernetics, NTNU. In 1999 she was a Visiting Fellow at the Department of Mechanical and Aerospace Engineering, Princeton University, Princeton, NJ. She has published more than 80 conference and journal papers. In 2006 she received the IEEE Transactions on Control Systems Technology Outstanding Paper Award. She is a senior member of IEEE and holds several board positions. Her research interests include nonlinear control of mechanical systems with applications to robotics, satellites, AUVs and ships.